Lakehead University

Knowledge Commons,http://knowledgecommons.lakeheadu.ca

2021

An enhanced Teager Huang transform technique for bearing fault detection

Chen, Zihao

An Enhanced Teager Huang Transform Technique For Bearing Fault Detection

By:

Zihao Chen

A thesis presented to the Lakehead University in fulfillment of the thesis

requirement for the degree of Master of Science in Mechanical Engineering

Lakehead University, Thunder Bay, Ontario, Canada

Abstract

Rolling element bearings are widely used in rotating machinery. Bearing health condition monitoring plays a vital role in predictive maintenance to recognize bearing faults at an early stage to prevent machinery performance degradation, improve operation quality, and reduce maintenance costs. Although many signal processing techniques have been proposed in literature for bearing fault diagnosis, reliable bearing fault detection remains challenging. This study aims to develop an online condition monitoring system and a signal processing technique for bearing fault detection. Firstly, a Zigbee-based smart sensor data acquisition system is developed for wireless vibration signal collection. An enhanced Teager-Huang transform (eTHT) technique is proposed for bearing fault detection. The eTHT takes the several processing steps: Firstly, a generalized Teager-Kaiser spectrum analysis method is suggested to recognize the most representative intrinsic mode functions as a reference. Secondly, a characteristic relation function is constructed by using cross-correlation. Thirdly, a denoising filter is adopted to improve the signal-to-noise-ratio. Finally, the average generalized Teager-Kaiser spectrum analysis is undertaken to identify the bearing characteristic signatures for bearing fault detection. The effectiveness of the proposed eTHT technique is examined by experimental tests corresponding to different bearing conditions. Its robustness in bearing fault detection is examined by the use of the data sets from a different experimental setup.

Acknowledgements

I have taken efforts in this thesis. However, it would not been possible without the kind support and help of many individuals.

First and foremost, I am indebted to Dr. Wilson Wang for his guidance, patience, and encouragement. I am heartily thankful for his genuine efforts to explore possible funding routes for the continuation of my research studies.

I would like to express my gratitude towards Dr. Xiaoping Liu, Dr. Sultan Siddiqui and Dr. Murari Roy for attending my thesis committee and providing helpful suggestions.

I would like to express my gratitude toward my parents, and my grandparents for their encouragement and constant support.

My thanks and appreciations also go to my colleagues Manzar, Toky , Hiren, and Jital for their support and advice in project development.

I also want to thank my friends: Hongli, Peter, Yichao, Youzuo, Haining, Amy and Yao for their generous support.

Table of Content

Table of Figures

Table of Tables

Chapter 1

Introduction

1.1 Overview

Rolling element bearings are commonly used in rotating machinery to support shaft rotation and loads. The unexpected bearing fault could create significant economic impact and safety risk in applications, such as aircraft, manufactory, water treatment plant, power generation [1]. According to investigation [2], more than half of small and medium-sized rotating machinery failures are directly related to unexpected bearing faults. Therefore, reliable bearing fault detection techniques are critically needed to recognize bearing defects at its earliest stage so as to enhance machinery performance, increase production efficiency, and reduce maintenance costs.

1.2 Condition Monitoring

Condition Monitoring (CM) is the process of measuring appropriate parameters of conditions in machinery to recognize any machinery deterioration that usually appears as a significant change in physical measurement (i.e., temperature, pressure, vibration, etc.). From system state perspective, CM can be described as evaluating current state and forecasting the future state of a system through physical measurements and mathematical modeling [3]. Fig. 1.1 illustrates a typical trend curve of deterioration within running time. An appropriate technology is needed to provide an early stage alert that could prevent failure by managing a repair or predictive maintenance during LEAD TIME.
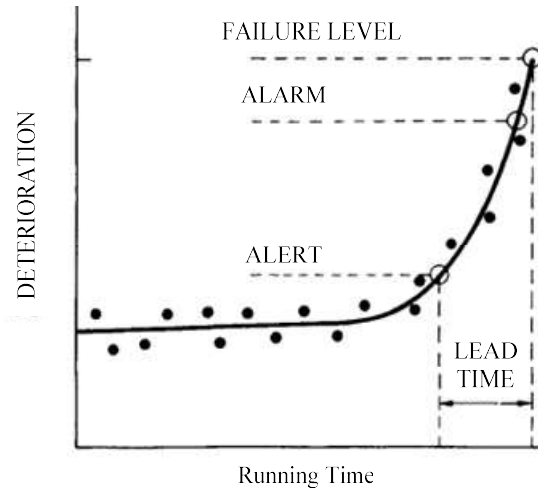
Figure 1.1. The principle of CM. which indicates the deterioration of the equipment (Reproduced from [4]),

In modern industry, a reliable health CM system can reduce loss by preventing downtime and improving equipment life cycle. [5] Figure 1.2 illustrates a typical CM system, which consists of three states: data acquisition (DAQ), signals processing, and fault diagnosis. First, the signals are measured from the related machinery by using appropriate sensors and the DAQ system. Second, fault-related features from the signal are extracted by using befitting signal processing techniques. The fault diagnostics is performed by categorizing the extracted features into different categories corresponding different machinery health states.
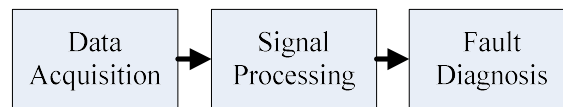
Figure 1.2: A flowchart of a machinery CM system

In general, machinery CM is undertaken offline, which requires experienced technicians to periodically measure data and do diagnostic analysis. Online CM is a diagnostic process, which can provide diagnosis results in real-time so as to prevent unnecessary machinery shutdown and unexpected safety incident, as well provide diagnostic information for troubleshooting in predictive maintenance. An online CM system may not recognize any immediate risk but can indicate excessive wear or notification of repairs and maintenance [6]. On the other hand, remote CM becomes the most efficient online CM, which allows the data retrieval and signal analysis to be performed at a different location. Moreover the dropping

price for the microcontroller unit (MCU) and transducer has made it possible to make smart sensors and wireless onboard DAQ systems [7].

1.3 The Data Acquisition System

A DAQ system can be used to make measurement of physical phenomena for CM analysis [8]. In the past decades, MCUs and electrical components have become cheaper, smaller in size and faster in processing. A smart sensor is a system to integrate the sensing units with onboard DAQ system, controlled by a MCU, for automatic data collection, preprocessing and wireless data transmission [9]. In 1984, Honeywell developed an air data transducer for aerospace applications, which could be the first commercial smart sensor device in the market [10].

A smart DAQ system consists of four major components: sensing units, signal conditioning, analog-to-digital converter (ADC), MCU, and DAQ control software. Figure 1.3 illustrates functional modules of a smart sensor node.
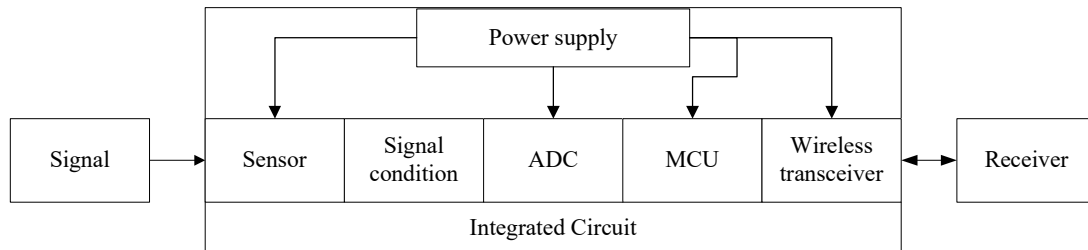
Figure 1.3: A block diagram of a classical integrated smart sensor system

A sensing unit is a device that detects and responds to different types of physical inputs from the surrounding environment, such as vibration, heat, pressure, light, and temperature. The sensor's output is a measurable analog electric quantity (e.g., voltage, current, charge) for displaying, transmitting, and further signal processing [11]. Signal conditioning is a fundamental building block of a DAQ device. The purpose of signal conditioning is to provide necessary functions for precise measurement, including electrical isolation, signal filtering, amplifier, offset adjustment, conformance with sensor requirements, etc. Electrical isolation is a process to reduce unnecessary noise and prevent ground loops in the measuring

chain. Electrical isolation is to separate the circuit from other electrical potential sources. In general, signals from the sensing units are relatively weak in magnitude, and external electrical potentials in both DC and AC forms can impact the signal significantly. For multi-channel DAQ systems, electric isolation is important from channel to ground, important from channel to channel. Signal amplification is the process of increasing the signal for processing or digitization.

In signal conditioning, there are different types of amplifiers for different purposes. Signal amplification can be performed either by increasing the input signal's resolution/magnitude, or by increasing the signal-to-noise ratio. For example, isolation amplifier is designed to isolate high DC levels from the device while passing small AC or differential signals [12]. Filtering is a processing function that some of signal frequency components, including noise, are filtered out based on requirements. There are several types of filters such as low-pass, high-pass, band-pass, and band-stop types. The filters can also be made from either passive or active components, as well as in analog and digital forms. For example, a passive filter only requires resistors, capacitors, and inductors with a maximum gain, while an active filter uses additional active components such as operational amplifiers. Unlike passive and active analog filters, the digital filter is a mathematical algorithm used to manipulate a signal with logic components.

The ADC is another important building block of the DAQ system. The ADC can convert the conditioned analog input to a digital output for display, storage, and advanced processing analysis. Successive approximation (SAR) and Delta-Sigma are common types of ADC functions in modern DAQ applications. SAR ADC can provide resolution up to 18 bits and sample rate up to 1MHz. Although SAR has no inherent anti-aliasing protection, it is still commonly used in ADC due to its balanced performance and low cost. Compared with SAR, Delta-Sigma ADC is more expensive, but has higher dynamic performance and inherent anti-aliasing protection with resolution up to 32bit, and the max sample rate of 1MHz [13].

DAQ software can provide necessary visualization, analysis and control functions in the DAQ system. Data storage strategy depends on application requirements. In some low power

wireless DAQ systems, signals are collected periodically with a relevant small sample number and then data are transferred to a PC or cloud [14,15]. Nowadays, flexible DAQ systems allow the user to visualize and check the data in real-time during data collection and to configure displays using built-in graphical widgets with common signal processing functions such as FFT and statistical analysis.

Wired DAQ systems have been commonly applied in industry applications [16]. However, the wired DAQ system is an objective reality, which is usually expensive in installation, maintenance. Most importantly, cabling setup may not be allowed in many industrial applications due to safety regulations or constrained space limitations. In contrast to the wired DAQ system, wireless smart sensor (WSS) could provide a balanced CM solution for machinery health CM and fault diagnostics. Depends on application requirements, several wireless communications can be applied, such as radio frequency (RF), ZigBee, WI-FI, and 5G.

To design a battery-operated WSS system for remote machinery CM, other specific requirements must be considered, including low power consumption, high ADC resolution and fast sampling frequency rate. The challenge in battery-operated WSS is related to the power-saving strategy and transmission robustness. The WSS should be controlled to enter some sleeping mode periodically and to transfer the data automatically and reliably without data missing.

1.4 Bearing Faults and the Characteristic Frequencies

Fig. 1.4 shows a typical rolling element bearing system. The rolling element bearing is a system that consists of components such as an external outer ring, an internal inner ring, a set of rolling elements, and a cage. There are many kinds of rolling element bearings in applications. For example, based on rolling element type, bearings can be classified into ball and roller bearings. Besides, based on carrying loads, bearings can be classified as radial load, axial load, and combined load bearings.
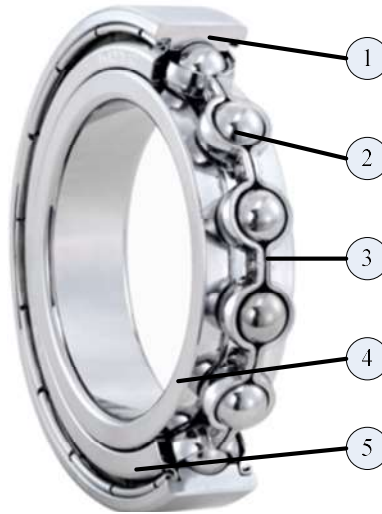
Figure 1.4: A rolling element bearing structure: (1) outer ring, (2) rolling element, (3) cage, (4) inner ring,(5) bearing seal.

In operation, a bearing acts as a source of vibration signal and noise. It is because a bearing carries loads by a finite number of rolling elements. The number of rolling elements and their position in the load zone make the bearing generate vibration signals even though the bearing is geometrically perfect and healthy. In applications, bearing materials are subjected to dynamic loading in operation. Localized defects (e.g., pitting and spalling) can be caused by dynamic stress on the races or the rolling elements [17]. Pitting/spalling is caused by material fatigue that cracks appear under the surface of the metal and propagates towards the surface until a small pit or spall drops off from the surface. Whenever a local defect on a bearing element directly contacts or indirect interacts with other bearing elements, brusquely changes in the contact stresses can generate a sharp pulse in a short duration, which will cause resonance vibration of the bearing components or bearing support structure.

Figure 1.5 illustrates the geometry of a ball bearing. Due to the bearing defect's unique characteristics, the vibration analysis becomes one of the most commonly used tools for bearing fault detection. Based on the defect location, the bearing defect results in different characteristic frequencies, which can be applied for bearing fault detection analysis.
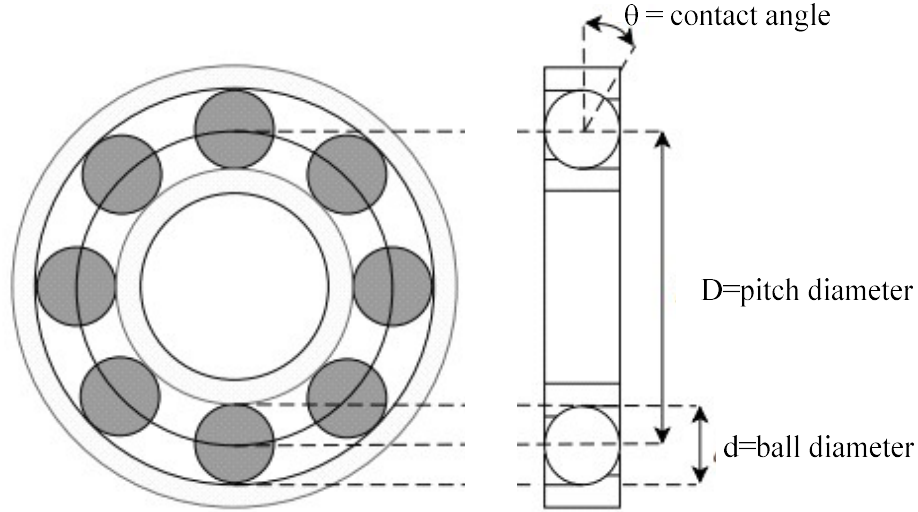
Figure 1.5: The geometry of a ball bearing [18]

The characteristic frequency for the bearing outer race defect is

$$f_{OD} = \frac{Z}{2}(1 - \frac{d}{D}\cos(\theta)) \times f_R \tag{1.1}$$

where Z is the number of balls, f_R represents shaft rotating speed (Hz), D is the pitch diameter, θ is the contact angle, and d is the diameter of the rolling element.

The characteristic frequency for the bearing inner race defect is

$$f_{ID} = \frac{Z}{2}(1 + \frac{d}{D}\cos(\theta)) \times f_R \tag{1.2}$$

The characteristic frequency for the bearing rolling element defect is

$$f_{BD} = \frac{D}{d}(1 - \frac{d^2}{D^2}\cos^2(\theta)) \times f_R \tag{1.3}$$

Usually, bearing dimensions can be found from the bearing data sheet or provided by the related manufacture according to the bearing type and product ID. One of the major challenges in detecting a bearing defect is that the resulting fault vibration signature is usually weak in magnitude and is masked by other higher-level vibratory signals. Moreover, the overbalance of the healing effect can be misleading in bearing fault detection [19]. Some early bearing failure indicators can be effaced in the late stages as the failure propagates. As

the defect propagates, the fault's overall energy increases, but usually becomes more wideband in nature. Therefore, to detect bearing fault reliably remains a very challenging task in this research and development field.

1.5 Time-Domain Analysis

The overall root-mean-square (RMS) of a signal can be an indicator representing signal energy related to bearing's health condition. RMS has been applied to detect localized defects with limited success in past research [20]. The RMS value continues increasing as bearing health conditions keep deteriorating [21]. It is expected that there could be a high value of RMS corresponding to an overall deterioration in a bearing system. However, this criterion may not always be the case in applications [22]. The crest factor in decibels is the difference between the peak and average of a signal, which can represent a signal's maximum peak to its RMS value. It is found that the crest factor can be used as an alternative measurement other than RMS level in vibration [23]. However, the crest factor is not a reliable fault indicator especially when the bearing fault feature is time-variant [24]. Generally, crest factor and RMS measurements can be used in identifying outrace defect that has time-invariant characteristics [22].

The amplitude probability density function (pdf) is insensitive to some variations of the signal pattern; as a result, its failure-related behavior for time versus amplitude can be used for machinery fault detection in some applications: the sharp peaks at the head will affect the pdf's tails.

The kurtosis is the fourth normalized moment of the pdf. Kurtosis function can be used to describe the "peakness" of the probability distribution of a random signal. The kurtosis value is around 3 for a healthy bearing with ideal Gaussian signal, and is greater than 3 for a faulty bearing when the signal becomes more non-Gaussian. However, the value of kurtosis will decrease or even get lower as the failure level propagates. This "healing" phenomenon can reduce the effectiveness of vibration-based fault detection [25]. The related investigation shows that applying kurtosis values at multiple frequencies are useful to help understand the

sensitivity of kurtosis in bearing failure [26]. This method does not need to know the historic information in the signal, and the health condition of bearing can be directly monitored by observing the kurtosis [27]. Although kurtosis-based analysis could provide reasonable fault detection in some applications, this method cannot be used reliably to detect an incipient failure [23], which is sensitive to factors such as load levels, speed fluctuation, and other conditions [28]. An improved indicator combining the kurtosis and RMS is suggested in [29] for bearing fault detection. The related indicators of RMS, kurtosis, skewness, and crest factor are tested for bearing fault detection in [30], which could be used with other soft computing method for bearing health CM.

1.6 Frequency-Domain Analysis

Signal characteristics can be analyzed in the frequency domain using techniques of the Fourier Transform (FT) in different forms such as the fast FT and the discrete FT. The power spectrum of a vibration signal after the FT can be used to examine the theoretical characteristic frequency components for bearing fault detection. The researchers in [31,32] find that the power spectrum cannot lose phase information between different frequency components. However the FT-based methods cannot be used for transient feature analysis [33]. It is found that those transient responses usually represent short term impulses due to bearing defects, which would generate a large number of low-frequency spectrums [34]. Furthermore, a general FT spectrum could contain disrupted spectral components that will interfere characteristic features and make it more difficult recognize defect-related frequencies for fault detection. Moreover, the FT-based methods can not capture the transient features of weak fault signals due to non-stationary nature.

Envelope demodulation can be used in bearing fault detection [35]. Envelope analysis of a band pass-filtered signal is a complementary tool to improve spectral analysis efficiency. Specifically, the signal is band-pass filtered to highlight the signals around the resonance of bearing fault characteristic frequency. Envelope analysis can be employed to detect structural defects that occur in machine components [35,36,37]. However, it is usually difficult to select

the proper frequency band of the band-pass filter for envelope analysis based on resonance frequency [38]. In [39], spectral kurtosis is applied to characterize non-stationary signals. A multi-scale enveloping spectrogram method is proposed in [40] for bearing defect diagnosis. Hilbert envelope and zero frequency resonator are combined in [41] for weak bearing fault detection. Envelope and cepstrum analyses are applied in [42] for machinery fault identification. Hilbert demodulation and bispectrum analysis are used for bearing fault detection in [42,43]. Cepstrum was introduced in [44] to investigate the periodic phenomena in frequency. Cepstrum is the inverse FT of the estimated logarithm spectrum; the peaks on the cepstrum correspond to the peaks in its frequency domain, which could identity outer race fault features but not the inner race fault [24].

1.7 Time-Frequency-Domain Analysis

Time-frequency-domain analysis is a signal processing technique that simultaneously allows studying a signal both in the time- and frequency-domain simultaneously. There are a variety of time-frequency signal processing approaches proposed in the literature, such as the discrete and continuous Wavelet Transform (WT) [45, 31, 33, 38], the short time FT [46], and the Hilbert-Huang Transform (HHT) [27,43,41].

Bearing race faults are detected by using discrete WT in [45]. Wavelets provide time-scale information of a signal, and can extract the features that vary in time, which makes WT a useful tool for non-stationary signal analysis. The continuous WT of a signal can resolve complex signals with its improved time-frequency localization properties. Unlike the continuous WT, the discrete WT has poor resolution in both the time-domain and the frequency-domain. Moreover, the WT has aliasing errors in decomposition due to its poor resolution [47].

The short-time FT is another time-frequency analysis technique; the chosen time windows will be transferred to the amplitude spectrum and repeated until all time-domain signals are processed. Although the resolution and accuracy of the short-time FT can be improved by increasing the overlap between each time window [46], its processing efficiency

decreases as the number of time windows increases. By adjusting the time window length and numbers can implement a precision trade-off. Hilbert Transfer is another time-frequency analysis technique that could extract instantaneous power and phase angles, both could represent the actual properties of the signal.

Based on the concept of Hilbert transform, the Hilbert Huang Transfer (HHT) can be used for analysis of nonlinear and non-stationary signals [48]. HHT operation takes two main steps: the first step is empirical mode decomposition (EMD) to decompose the original signal into a finite number of intrinsic mode functions (IMFs). In the second step, each IMF signal's phase is shifted 90 degrees to produce an orthogonal pair of signals. Each IMF signal and its associated orthogonal pair can be used to estimate the instantaneous variation in amplitude and phase angles. The HHT has been used for machinery fault detection research [49,50]. However, the HHT has some edge effect that can limit its accuracy, especially when the data length is too short. Therefore, large data size is usually required for HHT to extract instantaneous frequency components [51]. Another major shortcoming of EMD is the effect of mode mixing [48]. Mode mixing occurs when the oscillation with the same time scales occurs in different IMFs or the oscillations with disparate time scales are preserved in one IMF. To overcome the mode mixing problem, a noise-assisted ensemble EMD is proposed in [52].

The Teager-Kaiser (TK) energy operator is first proposed by Teager to calculate the energy for nonlinear sound production mechanisms [53, 54]. The TK energy operator only needs three samples for energy calculation at each instant time point, which can offer the advantages of high resolution, simplicity, and efficiency. Based on Teager's work in [53], Kaiser presents an algorithm in [55], to study a second order differential equation; it is observed that a simple sinusoidal signal's energy varies with both amplitude and frequency [56]. TK spectrum analysis has been used in nonlinear and non-stationary signal processing, for example, for wind turbine gearbox health analysis [57]. It has also proved the TK spectrum analysis has some merits over the Hilbert transform [58]. However, in machinery CM applications, the collected vibration signals contain significant background noise. From advanced investigation in our research team [59], it is found that the TK spectrum analysis is

very sensitive to high-frequency noise caused by reasons such as speed changes, power spikes, and sudden load.

1.8 Objective and Strategies

The objective of this MSc research work aims to extend the previous development in our research team, and develop a new CM system for online bearing fault detection.

The first objective is to improve a wireless DAQ system to collect both vibration and current signals. Zigbee and Wi-Fi wireless protocols will be tested for different communication applications.

The second objective is to propose a novel Teager Huang transform (THT) technique for non-stationary signal analysis and bearing fault detection in the outer race, inner race and rolling elements. The proposed enhanced Teager Huang transform (eTHT) technique is new in the following aspects: 1) a generalized Teager-Kaiser spectrum analysis is suggested to recognize the most representative IMF; 2) a correlation function method is proposed to choose some IMFs with the most representative features related to the bearing health conditions; 3) a denoising filter is adopted to improve the signal-to-noise-ratio, 4) the average spectrum analysis is undertaken to identify the bearing fault characteristic signatures for bearing fault detection. The effectiveness of the proposed eTHT technique is examined by experimental tests corresponding to different bearing conditions. Its robustness in bearing fault detection is examined by the use of the data sets from a different experimental setup.

1.9 Thesis Outline

This thesis is organized as follows:

Chapter 2 discusses a Zigbee-based wireless DAQ system and WiFi DAQ system development.

Chapter 3 conducts systematic comparison of the the denoising methods to extract impulsive features.

Chapter 4 discusses the proposed eTHT Technique.

Chapter 5 verifies the effectiveness of the proposed eTHT technique, with the comparison of other bearing fault detection techniques under different bearing testing conditions.

Chapter 6 summarizes the concluding remarks of this work and the future work to improve the current work.

Chapter 2

Development of Wireless DAQ Systems

This chapter aims to illustrate the development of wireless DAQ systems from our research team and my contributions. The development involves two types of wireless DAQ systems: a Zigbee wireless DAQ system, and a WiFi wireless DAQ system.

2.1 Zigbee-based Wireless DAQ System

Figure 2.1 illustrates the block diagram of the Zigbee-based wireless smart sensor DAQ system used in this research. This DAQ system consists of multiple smart sensor nodes and a receiver.

3.3 V					Smart Sensor Node
Voltage regulator	Sensing unit	Signal conditioning	MCU	ADC	(Tx) Wireless transceiver

3.3 V		Receiver
Serial-USB	MCU	(Rx) Wireless transceiver

9 V battery

Motor
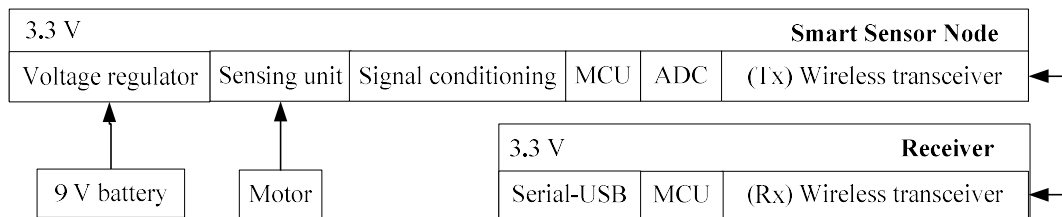
Figure 2.1: Block diagram of the Zigbee-based wireless smart sensor DAQ system.

2.1.1 A Smart Sensor Node

A smart sensor node is a combination of a sensing unit and intricate circuits, controlled by a microcontroller unit (MCU). Vibration sensing units or current sensing units can be applied based on requirements. The selected MCU is ATmega328P (from Microchip Inc) [60], which is a high-performance, low power, 8-bit AVR RISC MCU with a 32 kB in-system programming flash memory, 1024B EEPROM, 23 general purpose I/O lines, 2 kB static RAM (SRAM), and 10-bit built-in ADC. The output from the sensing unit gets filtered and amplified in the signal conditioning module before being digitized by the ADC module.

1) Analog-to-Digital Converter (ADC)

The ADC is referenced to a voltage-regulated output based on a battery power source. Equation (2.1) illustrates an ADC process:

$$x[n] = \left. \frac{V_{pin}(t)}{Q} \right|_{t = n/f_s} \tag{2.1}$$

where $V_{pin}(t)$ is the pin voltage, n is the sequence number of data, f_s is the sampling frequency, and Q is the analog quantization size, which can be expressed as:

$$Q = \frac{V_s}{2^b} \tag{2.2}$$

where V_s is the voltage of the power supply and b is the bit resolution of the ADC.

The changes of the analog quantization size by increasing the bit resolution can be considered a voltage value. For a voltage supply of 5 V, the quantization is $Q = 4.88\,\text{mV}$. The ADC can only recognize voltage changes larger than this quantization size.

2) Memory Extension

Atamaga328P has a 2 kB internal SRAM for data memory with an 8-bit data address architecture. Its data storage capacity is 2048×8 bits. In this development, extra data memory is required to store the ADC results. As shown in Figure 2.2, a 2×8-bit memory space is required to store each high-byte and low-byte values separately for each data point.
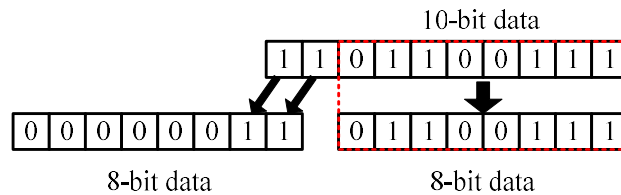
Figure 2.2: Storing 10-bit data in 8-bit memory locations.

The built-in ADC has a sample rate up to 15 KHz allowing only 1024 data samples to be stored. The data storage space is decreased further since the variables related to scripts and codes are also stored in the data memory. Since this amount is insufficient for machinery CM purposes, an external SRAM chip is required. The selected SRAM chip is 23LC1024 (from

Microchip Inc.) [61], which is a 128 kB SRAM that can store 64000 data samples.

3) Radio Frequency Communication

The selected transceiver in this project is CC1101 (from Texas Instruments) [62]. It is a low-cost sub-1 GHz transceiver with a maximum programmable data rate of 600 kbps, with a 200 nA sleep mode current consumption. The frequency range selected in this work is in the ultra-high frequency band at 915MHz. The module is powered by a 3.3V power supply. A voltage regulator is needed to drop the voltage from 5V to 3.3V. A customized version of the Simple Wireless Abstract Protocol (SWAP) [63] will be used to reduce transmission overhead and power consumption.

CC1101 chip data is received and transmitted in packets. Figure 2.3 illustrates the data structure for data transmitting. One packet consists of 64 bytes. The first byte represents the transceiver ID, which is used to synchronize the smart sensor node and the receiver. The second byte address is reserved for the packet number j. The first 10 bits of the data are stored in byte 3 and byte 4. Each 2 bytes can store one 10-bit data. Therefore, there are a total of 31 10-bit data that can be transmitted in one packet. The smart sensor node can sample up to $N = 16384$ ADC readings with an external SRAM. The smart sensor node can complete the wireless transmitting with $N/31=529$ packets.
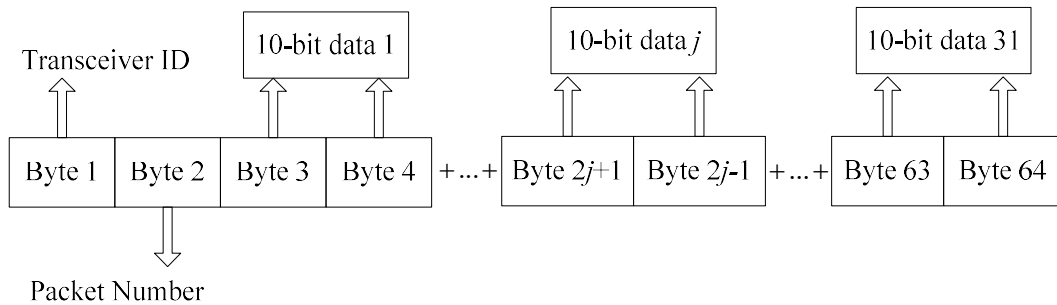
Figure 2.3 Wireless packet structures for CC1101 data transmitting

4) Serial-Peripheral-Interface (SPI) Protocol

The Serial-Peripheral-Interface (SPI) protocol is used for rapid chip-to-chip

communication in this project. Figure 2.4 illustrates the SPI connection scheme. The selected SRAM and wireless transducer are connected to the MCU as a slave device through the SPI protocol. The MCU is assigned as the master device to control the SRAM and wireless transducer. SPI communication has four lines: MISO (the master input slave output) mode and MOSI (the master output and slave input) mode. The clock signal (SCLK) for the SPI, which is usually provided by an external crystal oscillator. The chip select signal (SS) is used to select the slave device.
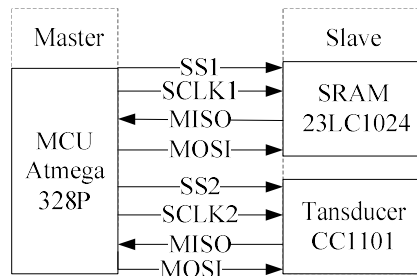
Figure 2.4: SPI connection scheme for Atmega328P.

5) Sleep Modes

The smart sensor node of the DAQ system is designed to be powered with batteries to collect signals. The power consumption of the DAQ system is a crucial indicator for its proper operation. The overall power consumption can be reduced by introducing a sleep mode for smart sensor nodes when no data collection is required. The MCU Atmega328P offers a selection of power modes. The power consumption can reduce from 16 mA in active mode to 0.04 mA in power-down modes. The ADC and wireless communication unit are disabled before the MCU entering the sleep mode. Those units require separate handling in code and proper arrangement. When the MCU enters the power-down mode, the regular operation can be resumed by triggering external interrupts. The wireless module is powered off in the power-down mode, so that the built-in external interrupt pin is disabled. Therefore, a watchdog timer (WDT) is introduced to trigger an internal interrupt to wake up the MCU. WDT is a timer module with a separate on-chip 128 kHz oscillator designed to limit the maximum time allowed for the power-down mode.

2.1.2 The Receiver System

Figure 2.5 illustrates the block diagram of the developed receiver unit. The receiver unit mainly consists of two parts: a wireless transceiver and an MCU. The selected MCU is also the Altamage328P. The selected wireless transducer is CC1101, which is the same as that used in the smart sensor node setups. A USB protocol is introduced for serial communication and power supply purposes. After the data is transmitted from smart sensor node, the data can be uploaded to a PC by using serial communication. No extra SRAM is needed to store the data in the receiver.
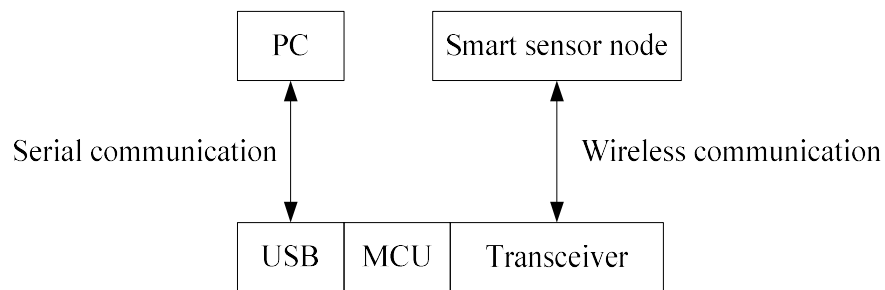
Figure 2.5: Receiver block diagram.

1) Handshake Protocol

The DAQ system adopts a handshake protocol for wireless data communication to prevent packet loss. The handshake protocol operates on the principle of validating the transmission of each data packet by the receiver. As illustrated in Figure 2.6, the receiver requests the data based on the packet number of each packet. When the smart sensor node receives the request, packet j is transmitted. Suppose the smart sensor node does not receive the request. The receiver will continuously request packet j until the packet arrives. The receiver has the same procedure to receive packets.
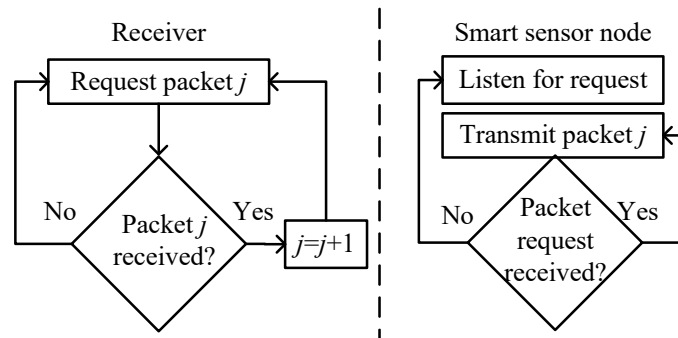
Figure 2.6: The handshake protocol.

2.1.3 The Related Development Project:

It would state that this smart DAQ system project is a team work. My main contribution in the development of Zigbee-based DAQ system is mainly related to programming. With the existing hardware setup and functionalities, multiple new functions are developed to improve the system operations. A data pre-processing program is made to transfer hex data into decimal in Visual Basic (VB). Multiple data relation features and functions are developed for multiple sensor nodes data collection, related to data collecting function, data transmission and auto-acquisition function, as illustrated below:

1) Data Pre-Processing

Data pre-processing program is developed to transfer hex data into decimal in PC after serial communication. As illustrated in Figure 2.7, data transmission begins with a packet indicator. Firstly, the strings of packet numbers need to be removed. Every content deleting procedure will result an empty string in the array. Then, all the empty strings from packets must be removed to ensure the data continuity. When there is only one value in the high-byte string, the string will be replaced by adding a leading 0. The next step is to combine each high-byte of hex data with its low-byte hex data to form a 16-bits hex data. Finally, the 16-bits hex data is transferred into a decimal value to be displayed and plotted.
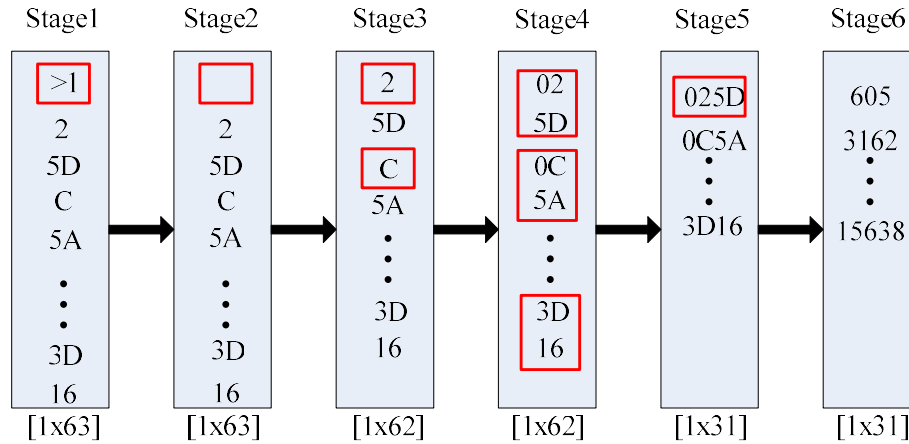
Figure 2.7: Six stages of hex to decimal data transforming for data pre-processing.

2) Data Collection

Figure 2.8 illustrates the system diagram of the data collection function for two smart sensor nodes. Firstly, the receiver (R1) sends a command to build a handshake with the first smart sensor node (T1). When T1 receives the command, it sends an acknowledgment back to R1 and starts to collect data simultaneously. At the same time, T1 will send out a message to the DAQ system, and inform R1 to become R2. Then receiver R2 will build a handshake connection with the second sensor node T2. T2 sends an acknowledgment back to R2 and starts collecting data. Whenever a smart sensor node finishes data collection, a flag will be generated in the program. When data collecting is completed for all smart sensor nodes, the program will display a message based on those flags and indicate that all the data are collected and saved in the SRAM. Proper delay functions need to be added to optimize the program processing time.
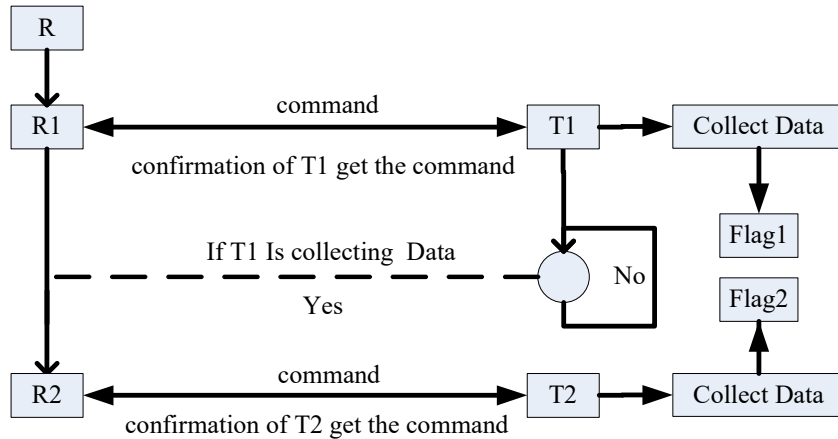
Figure 2.8: System diagram of data collection

3) Data Storage

At the end of the data collection process, a function of data saving is required to secure data storage on a PC. Figure 2.9 illustrates the system diagram of the data saving function of two smart sensor nodes. Upon begging, the receiver R1 sends commend to T1 to transfer data wirelessly. If the data is transferred successfully, the hex data will be changed into decimal data automatically. The related file destination and name will be automatically created, and the data will be saved on the PC. The program has a functionality to identify the data saving progress and send a command to R1 for next sensor node's wireless data transmitting. After receiver R1 has got the command, R1 changes into R2 and asks the next smart sensor node T2 to transfer the data wirelessly. The previous steps will be repeated for other smart sensor nodes. After all the collected data are successfully saved on the PC, receiver R2 will send a command to the smart sensor node T2 to enter a sleep mode to save power. Sleep periods depend on monitoring applications. Before T2 enters sleep mode, T2 will send a message back to the receiver until T2 gets an acknowledgment back from the receiver. This step is essential to ensure the receiver has realized that the smart sensor node is entering a sleeping mode to avoid smart sensor nodes operating in the sleeping period. Then receiver R2 will become R1 to build a handshake with another smart sensor node T1 following the previous steps to let T1 enter a sleeping mode.
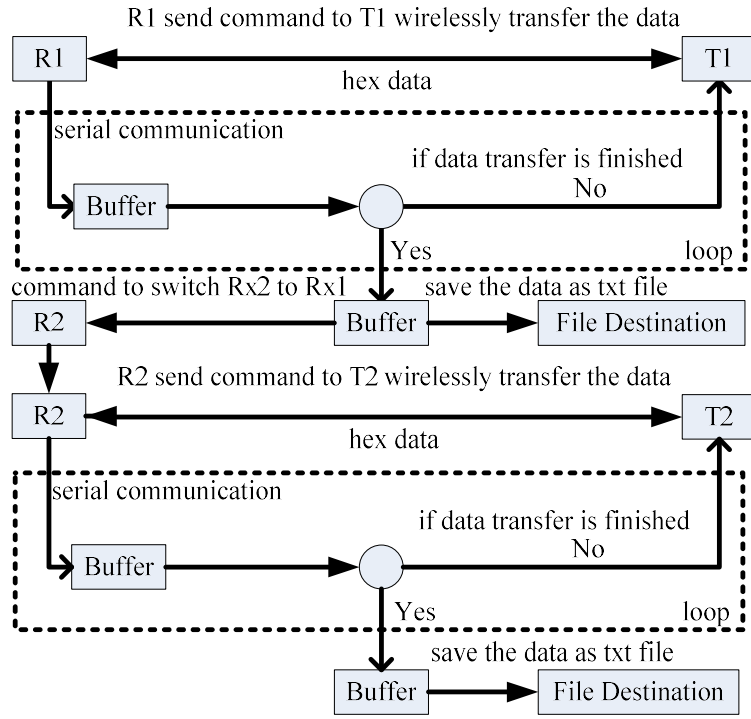
Figure 2.9: System diagram of data storage

4) Auto Data Acquisition

The auto-acquisition program is developed based on the need of automatic machinery condition monitoring. After each smart sensor node has collected data, the operating system should periodically enter sleep mode to reduce power dissipation. Figure 2.10 illustrates the real-time data acquisition cycle with three major steps: 1) active smart sensor nodes collect signals; 2) smart sensor nodes upload data; 3) smart sensor nodes enter sleep mode to save power. The above steps will be repeated until the DAQ operations are finished or the battery power level is not high enough. This program is based on the combination of data collection function and data storage function. The selected wireless transducer C1101 has a maximum sleeping mode time of 8 seconds. After 8 seconds, the system has to be reset. If the goal of sleeping time is 4 hours, it required 14400 / 8sec = 1800 times resetting in each sleeping period. Moreover, it is necessary to ensure the flag of resetting times cannot be erased after resetting. Therefore, an erasable programmable read-only memory (EPROM) is used in the circuit. The flag can then be added up for each reset by circuit power down or resetting functions.
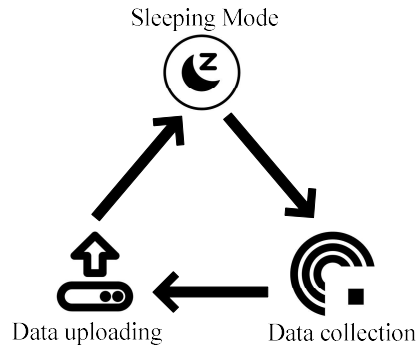
Figure 2.10: Auto data acquisition cycle.

The effectiveness of the auto-acquisition function has been tested and verified in our research lab. It can operate automatically with a 4-hour sleep period for a total of approximately 32 hours. Figure 2.11 shows the data collected in text files by one smart sensor node. The file destination is automatically generated by the program with a formula of Autosensor#i-j.txt, where i represents the identity of the smart sensor node, and j denotes the identity of data. The time in date modified shows a 4-hour gap between each data file. The size section indicates that all the data files have the same size of 18 kB. The size of the data file depends on the data collected and data type. Proper delay functions are needed to improve the operation stability and avoid data inconsistency.

Name	Date modified	Type	Size
Autosensor#1-0.txt	3/1/2020 4:24 PM	Text Document	18 KB
Autosensor#1-1.txt	3/1/2020 8:25 PM	Text Document	18 KB
Autosensor#1-2.txt	3/2/2020 12:26 AM	Text Document	18 KB
Autosensor#1-3.txt	3/2/2020 4:27 AM	Text Document	18 KB
Autosensor#1-4.txt	3/2/2020 8:28 AM	Text Document	18 KB
Autosensor#1-5.txt	3/2/2020 12:28 PM	Text Document	18 KB
Autosensor#1-6.txt	3/2/2020 4:29 PM	Text Document	18 KB
Autosensor#1-7.txt	3/2/2020 8:30 PM	Text Document	18 KB
Autosensor#1-8.txt	3/3/2020 12:31 AM	Text Document	18 KB

Figure 2.11: Auto data collection in text format over 32 hours.

5) User Interface

A user interface (UI) has been developed in VB for the wireless DAQ system, which could be used in the monitoring system in the Bare Point Water Treatment Plant in Thunder Bay. Figure 2.12 shows an overview of the UI. The serial display displays instructions for

smart sensor nodes and some functionality from execution. The connection panel is used to detect and activate USB connection between the receiver and a PC. The data collection panel is designed to control the measurement process. The *Data Store to SRAM* button can be used to manually save the data to the SRAM on the smart sensor node. The *Wirelessly Transfer Data* button can manually transfer data from the smart sensor node to the receiver. The *Auto Data Collection* button can automatically conduct the data collection and enter sleep mode based on a selected period. The *Auto Exit* button is implemented to quit the *Auto Data Collection* process. The sensor panel has two buttons: *Sleep* button will let the smart sensor node enter a sleeping mode; *Reset* button is used to restart the smart sensor node. The status bar is designed to show the percentage of progress during signal execution.
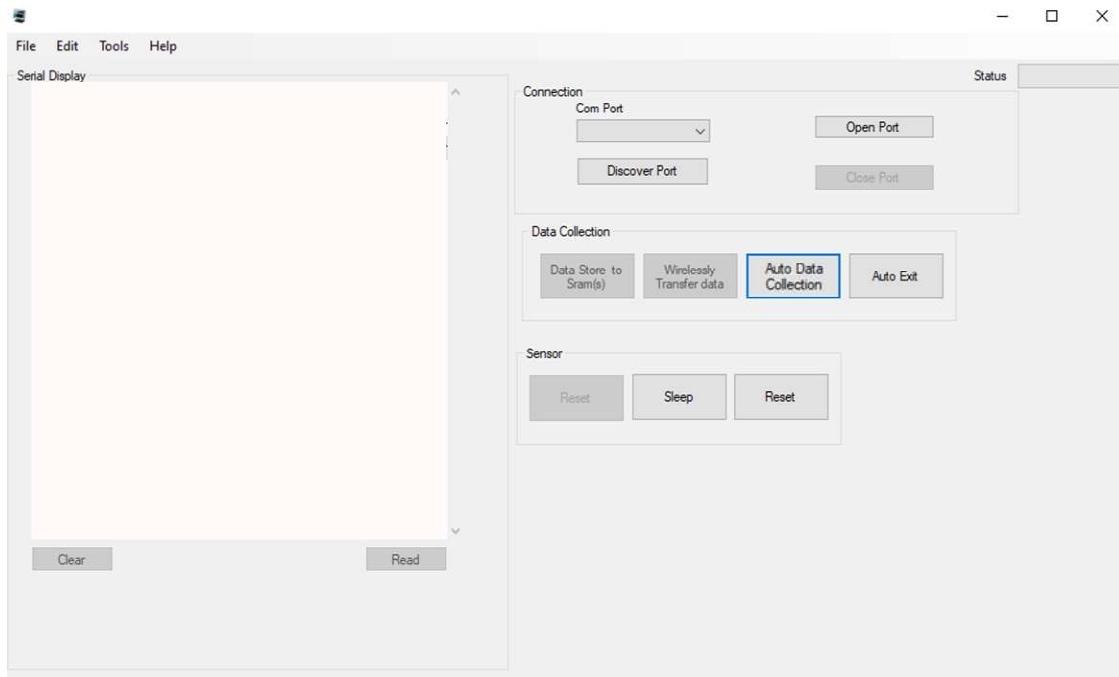
Figure 2.12: An user interface for Zigbee-based DAQ system

2.2 A Wi-Fi DAQ System

As Zigbee wireless protocol is used, the wireless signal will be weakened by a wall and other obstructions between the data transmission path, especially under high-noise environment. Therefore, an alternative solution of using Wi-Fi protocol will be developed for another smart DAQ system, which can be used for applications where WiFi servers are

available like in the Bare Point Water Treatment Plant. But the main challenge in using the Wi-Fi protocol in a standalone monitoring system is related to its large power consumption. Wi-Fi system generally consumes 400% of the power of Zigbee-based system. Or if a Zigbee system that can operate over 32 hours with a battery, the Wi-Fi DAQ system can only last about 8 hours. Therefore, the main challenging issue in design and building a battery-powered Wi-Fi DAQ system is how to reduce power consumption.

2.2.1 A Wi-Fi Smart Sensor Node

In a Wi-Fi smart DAQ system, the receiver hardware as illustrated in the aforementioned ZigBee systems is not required. Smart sensor nodes can send data directly to a cloud or a PC. A standalone Wi-Fi smart DAQ system also requires a battery power supply. Extra storage is required to store the data. A 24-bit ADC chip is introduced in this development project to improve the ADC resolution. Figure 2.13 illustrates the main elements of a Wi-Fi smart sensor node.
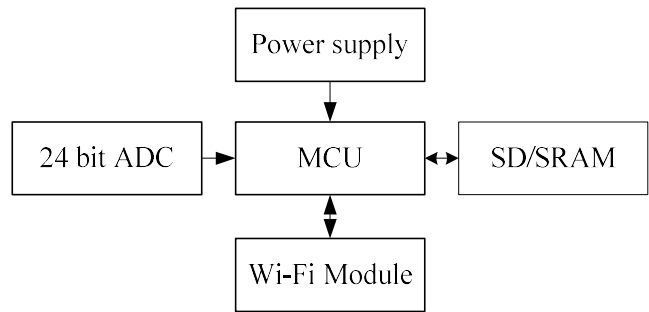
Figure 2.13: Wi-Fi smart sensor node block diagram.

2.2.2 ESP32-S2 Microcontroller

The selected MCU is the ESP32-S2 from ESPRESSIF Inc. [64]. This MCU has an integrated Wi-Fi connectivity and is developed based on ESP8266, which has been used in Internet of Things (IoT) applications. The ESP32-S2 is an ultra-low power consumption device (22 mA current consumption when it operates at 240 MHz), which supports multiple sleep modes. Moreover, if ESP32-S2 is operating at 80 MHz, the current consumption of ESP32-S2 will drop to 14mA, which is even less than the Atmaga328P MCU. The

supported sleep modes are listed in Table 2.1.

Table 2.1: ESP32-S2 Sleep modes table.

Work mode	Description		Current consumption
Modem-sleep	The CPU is powered on	240 MHz	22 mA
		160 MHz	17 mA
		Normal speed: 80 MHz	14 mA
Light-sleep			550 µA
Deep-sleep	The ULP co-processor is powered on.		235 µA
	ULP sensor-monitored pattern		22 µA @1%duy
	RTC timer+ RTC memory		25 µA
	RTC timer only		20 µA

The unique sleeping mode features make ESP32-S2 the ideal MCU chip for this battery-powered wireless DAQ system. ESP32-S2 can be used in general industrial applications at temperatures between -40°C and +125°C. With a built-in Wi-Fi module in the ESP32-S2, the design and PCB development become more straightforward and cheaper. Figure 2.14 shows an ESP 32-S2 smart sensor node block diagram, and Table 2.2 summarizes some essential features of this MCU.
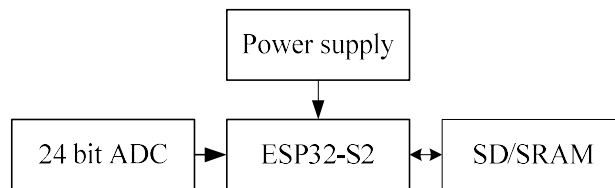
Figure 2.14: Wi-Fi smart sensor node with ESP32-S2.

Table 2.2: ESP32-S2 feature table.

ESP32-S2	
CPU	Single-Core LX7
SRAM	320 KB
ROM	128 KB
EXT SPI-Ram Support	128 MB
EXT SPI-Flash Support	1 GB
GPIOs	43
Operation Speed	80 MHz, 160 MHz, 240 MHz
Wi-Fi	802.11 b/g/n and TOF (Time of Flight)
LCD	8/16/24-bit parallel RGB/8080/6800
USB	Full Speed USB OTG
SPI	4

2.2.3 The 24-Bit ADC Chip

The selected external high-speed ADC chip is the ADS131A04 (from Texas Instruments) [65]. It is a four-channel, 24-bit Delta-Sigma ADC with speed up to 128-kilo samples per second (ksps). ADS131A04 has a flexible analog power supply option and can be powered by a unipolar supply between 3.3 V and 5.5 V. It can also be powered by a bipolar supply from -2.5 V to +2.5 V. ADS131A04 also has a unique high-speed SPI interface to communicate with other chips. The ADS131A04 has three main operation modes of asynchronous interrupt, synchronous master, and synchronous slave as illustrated below:

1) Asynchronous Interrupt Mode

Figure 2.15 depicts the relevant device connection using ADS131A04. The asynchronous interrupt is the preferred mode for the operation of a single device. In this mode, a unique Data Ready (DRDY) pin is used to interrupt the master device to read the conversion data.
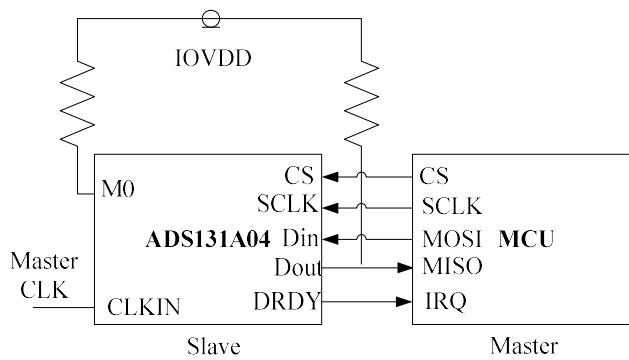
Figure 2.15: Asynchronous interrupt mode connection.

2) Synchronous Master Mode

The relevant device connection of ADS131A04's synchronous master mode is illustrated in Figure 2.16. The synchronous master mode can be used with ADS131A04 as the master device. MCU is used as a slave device to read data after each conversion.
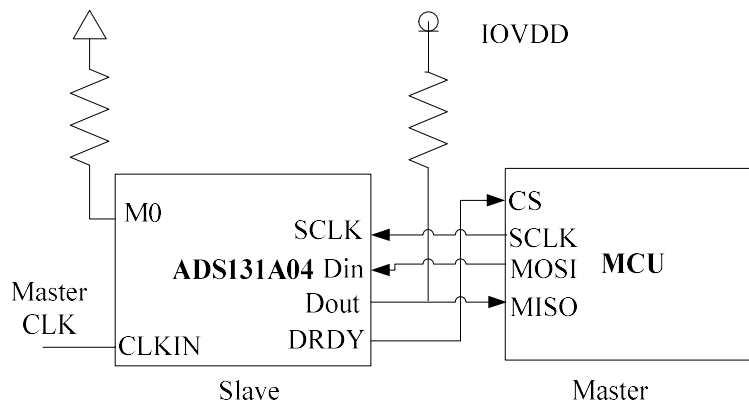
Figure 2.16: Synchronous master mode connection.

3) Synchronous Slave Mode

Figure 2.17 represents the device connection of ADS131A04 in synchronous slave mode. Synchronous slave mode can be used when there exist a synchronous master clock and a master to control the slave device. This mode is usually used for controlling multiple slave devices by one master device.
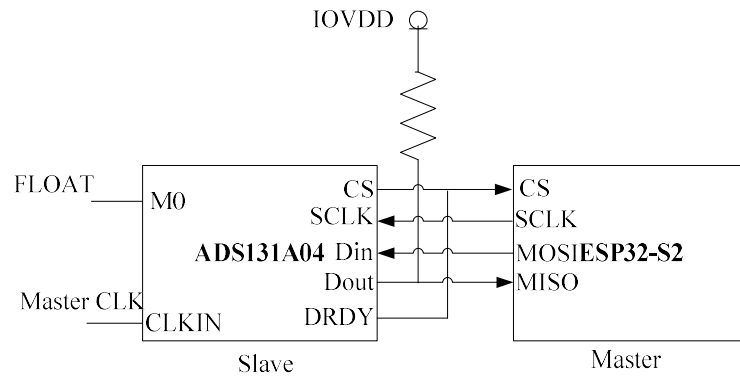
Figure 2.17: Synchronous slave mode connection.

Chapter 3

Signal Denoising Filtering

Whenever a defect occurs on a bearing component, the impact between the damaged area and other bearing components will generate impact impulses. Then the impulses are transmitted to the bearing housing, to the housing structure, up to the measurement sensor. Characteristic defect features will be modulated by impedance during this transmission path, as well as background noise. Denoising is a filtering process of reducing impedance related to the signal transmission path so as to improve the signal-to-noise-ratio (SNR) before advanced analysis for bearing fault detection.

There are several types of denoising filtering techniques proposed in literature. Autoregressive (AR) filter has been adopted for gear tooth fault detection [66]. Minimum entropy deconvolution (MED) based filter techniques have been successfully applied for gear tooth and bearing fault diagnosis [67,68,69,70]. However, for different signal dynamics, the performance of denoising filters varies. This chapter will illustrate the denoising filter's capability of impulse feature extraction. All of the related filtering techniques are programmed in MATLAB 2016b for testing and analysis.

3.1 Autoregressive Filtering

An AR filter is a process in which its current model output can be predicted based on its previous variables' linear combinations [71]. Figure 3.1 illustrates the procedure of an AR denoising filtering. Where $x(n)$ is the input signal with impulsive features, $\hat{x}(n)$ represents the results predicted by the AR model, and $e(n)$ is AR prediction error.

$x(n)$ — Inverse AR Model of noise — $\hat{x}(n)$ — Σ — $e(n)$

$x(n)$
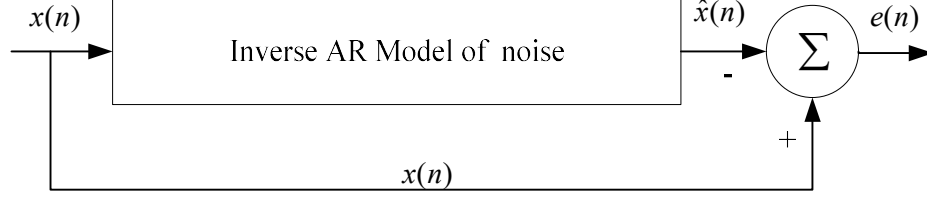
Figure 3.1. Illustration of AR filtering.

Consider a discrete time series $\{x_i\}$, the predicted AR process can be represented as

$$x_{i+1} = \sum_{i=1}^{N} \phi_i(x_i) + \xi_{i+1} \tag{3.1}$$

where x_{i+1} is the goal, $\sum_{i=1}^{N} \phi_i(x_i)$ represents the sum of previous Nth variables, ϕ_i is the numeric coefficient of the corresponding lagged variable x_{i-1}, ξ_i denotes random perturbation, and N is the order of the AR model.

Multiplying a lagged variable x_{i-1} on both sides of Equation (3.1) yields

$$x_{i-1} x_{i+1} = \sum_{i=1}^{N} \phi_i(x_i x_{i-1}) + x_{i-1} \xi_{i+1} \tag{3.2}$$

Eliminating the zero-correlation term from Equation (3.2) yields:

$$r_{xx}[m] = \sum_{i=1}^{\beta} \phi[i] r_{xx}(m-i) \tag{3.3}$$

where r_{xx} is the auto covariance function of x_i and x_{i+1}, $m = 0, 1, 2,\ldots, \beta$.

Then, Equation (3.3) can be expressed in the following matrix representation for $m > 0$:

$$
\begin{bmatrix} r_0 \\ r_1 \\ \vdots \\ r_{N-1} \\ r_N \end{bmatrix}
=
\begin{bmatrix}
r_0 & r_1 & r_2 & \cdots & r_{N-2} & r_{N-1} \\
r_1 & r_0 & r_1 & \cdots & r_{N-3} & r_{N-2} \\
\vdots & \vdots & \vdots & \vdots & \vdots & \vdots \\
r_{N-1} & r_{N-2} & r_{N-3} & \cdots & r_0 & r_1 \\
r_N & r_{N-1} & r_{N-2} & \cdots & r_1 & r_0
\end{bmatrix}
\begin{bmatrix} \phi_1 \\ \phi_2 \\ \vdots \\ \phi_{N-1} \\ \phi_N \end{bmatrix}
\tag{3.4}
$$

Therefore, the inverse AR model can be represented as:

$$\boldsymbol{\phi} = R^{-1}\boldsymbol{r} \tag{3.5}$$

where $\boldsymbol{R}$ is the square coefficient matrix, and $\boldsymbol{r}$ represents the autocorrelation sequence.

Figure 3.2 shows the comparison of some processing results by using the AR filter with different noise conditions. In Figure 3.2 (b), the simulated impulsive signals are buried in white noise with the different noise levels. It is seen from Figure 3.2 (c)-(f) that the AR filter fails to recognize impulsive signals only if the noise level becomes lower than 60% in this case, as shown in Figure 3.2(e)(f) with (i.e., 60% and, 40% of its original magnitudes).
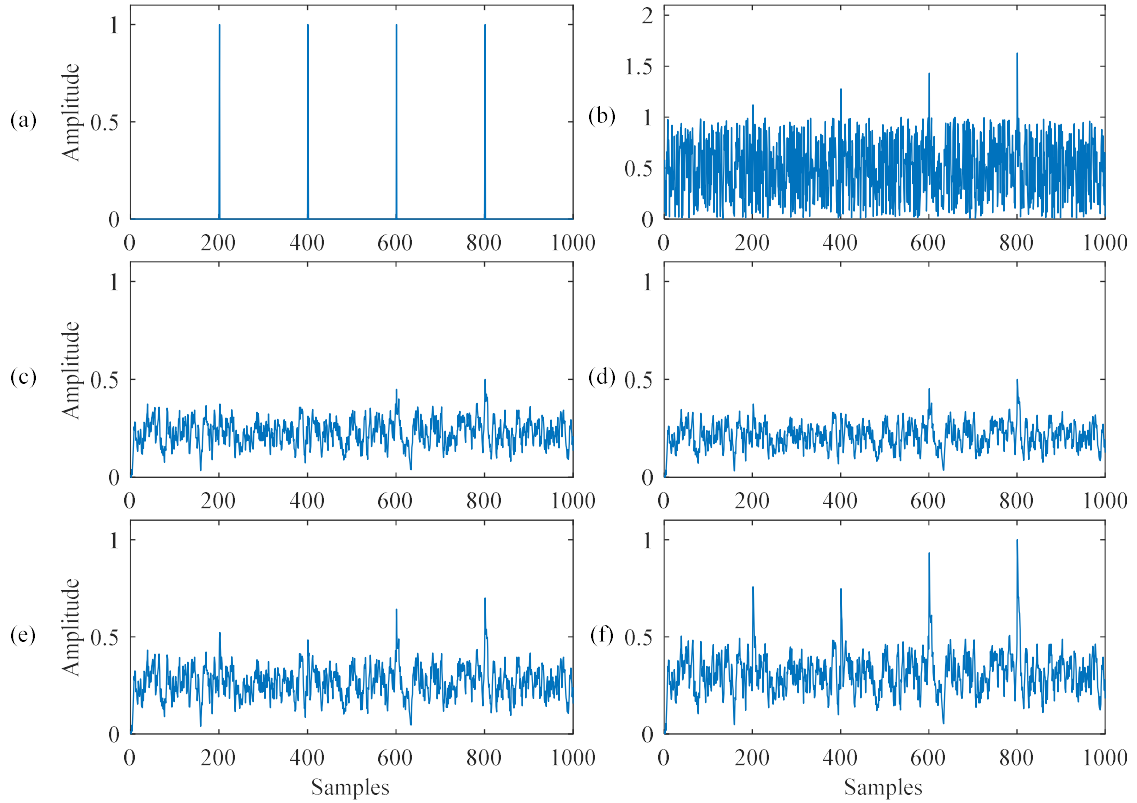
Figure 3.2: Comparison of the processing results using the AR denoising filter corresponding to different noise levels: (a) Simulated impulsive signal, (b) impulsive signal with noise, (c) processing result with 100% noise level, (d) processing result with 80% noise level, (e) processing result with 60% noise level, (f) processing result with 40% noise level.

3.2 MED Filtering

The MED filter proposed in [72] is to deconvolute the impulsive signatures from the

collected signals to highlight impulse features, which can be used for machinery health condition monitoring.

Figure 3.3 illustrates the processing procedure of the MED denoising filtering. If $q(n)$ represents a source signal and $h(n)$ denotes disturbance of the transmission path, then the input signal $x(n)$ is defined as:

$$x(n) = h(n) \otimes q(n) + e(n) \tag{3.6}$$

where $\otimes$ denotes the convolution operator, and $e(n)$ represents the noise.
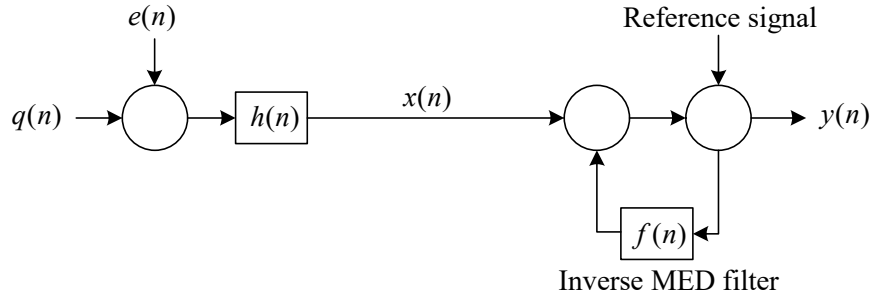
Figure 3.3: Illustration of MED filtering.

Suppose that the signal $x(n)$ is convolved with the MED filter $f(n)$, the output $y(n)$ will be

$$y(n) = f(n) \otimes x(n) = f(n) \otimes h(n) \otimes q(n) + f(n) \otimes e(n) \tag{3.7}$$

The filter coefficients in $f(n)$ can be optimized to recognize the impulsive signal by minimizing the entropy. The kurtosis K_{u2}^{4} of the signal can be expressed as:

$$K_{u2}^{4}(f(l)) = \frac{\sum_{i=1}^{N} y^{4}(i)}{\left(\sum_{i=1}^{N} y^{2}(i)\right)^{2}} \tag{3.8}$$

where $y(i)$ is the output after the inverse MED filter $f(n)$, l represents the delay and N is

the length of the signal.

The optimal inverse MED filter coefficients can be achieved by maximizing $K_u(f(l))$, such that:

$$\frac{\partial(K_{u2}^4(f(l)))}{\partial(f(l))} = 0 \tag{3.9}$$

The convolution of the inverse MED filter can be expressed as:

$$y(i) = \sum_{i=1}^{L} f(l)z(i-l) \tag{3.10}$$

where L is the filter length, z is the observed signal, and l is the delay. The partial derivative of Equation (3.10) can be expressed as:

$$\frac{\partial(y(i))}{\partial(f(l))} = z(i-l) \tag{3.11}$$

Combining Equations (3.9), (3.10), and (3.11) yields:

$$\frac{\sum_{i=1}^{N} y^4(i)}{\sum_{i=1}^{N} y^2(i)} \sum_{i=1}^{N} y^3(i)z(i-l) = \sum_{p=1}^{L} f(p) \sum_{l=1}^{N} z(i-p)z(i-l) \tag{3.12}$$

Based on Equation (3.12), the iterative $f(p)$ can be expressed as:

$$B = A \times f \tag{3.13}$$

where $B = \dfrac{\sum_{i=1}^{N} y^4(i)}{\sum_{i=1}^{N} y^2(i)} \sum_{i=1}^{N} y^3(i)z(i-l)$ is the left-hand side of Equation (3.12); $A=$

$\sum_{l=1}^{N} z(i-p)z(i-l)$ is the $L \times N$ autocorrelation matrix of the observed signal and f is the filter coefficients.

After several iterations, the filter coefficient f can be calculated as:

$$f = (AA^T)^{-1}B \qquad (3.14)$$

Changing the MED filter length L from Equation (3.5) can provide different filtered results. Figure 3.4 compares the processing resulting from using the MED filter with different filter lengths. Figure 3.4(a) represents the simulated impulse signals; Figure 3.4(b) depicts the simulated impulsive signals with Gaussian white noise; and Figure 3.4(c), (d), (e), and (f) corresponds to MED-filtered results corresponding to filter lengths of 50, 100, 150, and 200 respectively.
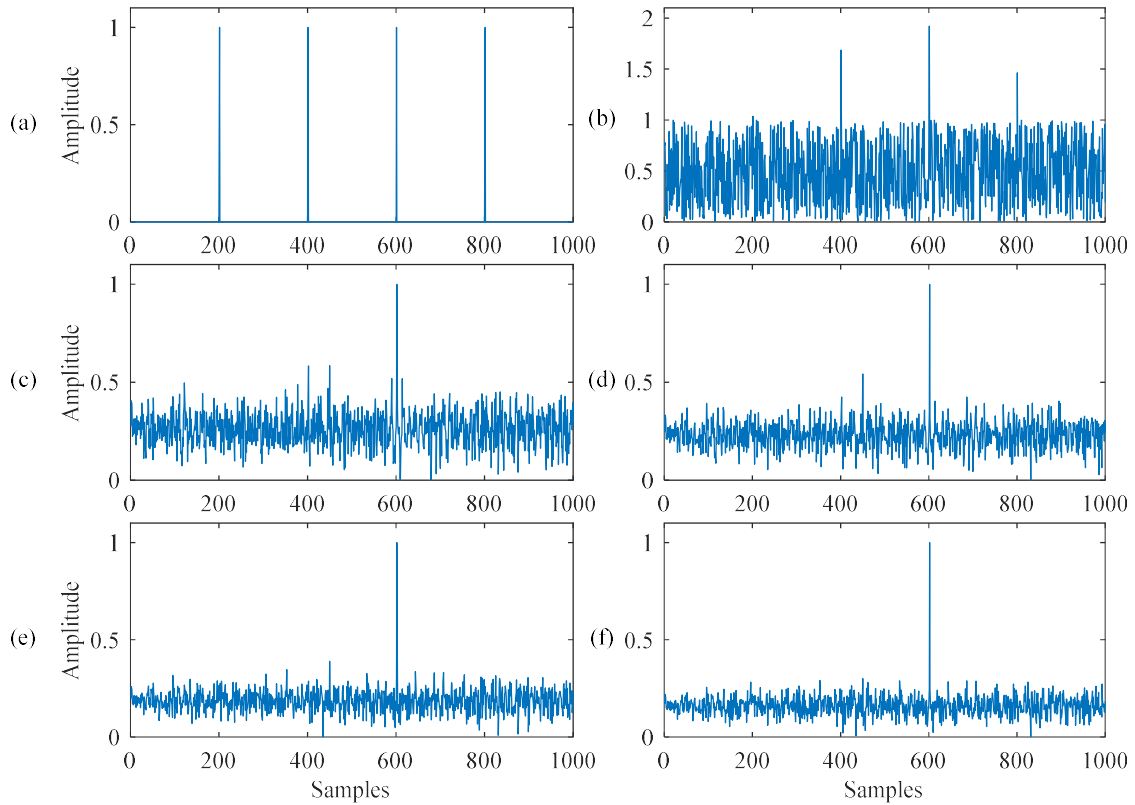
Figure 3.4: Comparison of MED-filtered results at different filter lengths: (a) Simulated impulsive signal, (b) impulsive signal with noise, (c) MED-filtered result with filter length $L = 50$, (d) MED-filtered result with $L = 100$, (e) MED-filtered result with $L = 150$, (f) MED-filtered result $L = 200$.

In this experiment, all the simulated impulsive signals from Figure 3.4(a) have the same magnitude as the maximum magnitude of random white noise. The results from Figure 3.4(c)-(f) indicate that with the incensement of MED filter length, the MED filter can only recognize single impulsive signal which is located at $t = 600$. Among the four simulated

impulsive signals, the impulsive signal with higher amplitude can be clearly recognized.

3.3 OMED Filtering

A new norm deconvoluting impulses called the D-norm is firstly proposed in [73] to solve the deconvolution problem, which is geometrically similar to the MED problem. The D-norm is defined as:

$$D(\vec{y}) = \max_{k=1,2,...,N} \frac{|y_k|}{\|\vec{y}\|} \tag{3.15}$$

where $\vec{y}$ represents the vector form of a discrete-time series, $|y_k|$ is the absolute value of the kth value in vector $\vec{y}$, and $\|\vec{y}\|$ is the norm of vector $\vec{y}$, which is defined as:

$$\|\vec{y}\| = \sqrt{\sum_{k=1}^{N} y_k^2} \tag{3.16}$$

The D-norm devonvolution can use a non-iterative algorithm such as the Optimal Minimum Entropy Deconvolution (OMED) to solve the filter coefficients. The OMED method can be formulated as the following:

$$\sup_{\vec{f}} D(\vec{y}) = \sup_{\vec{f}} \left(\max_{k=1,2,...,N} \frac{|y_k|}{\|\vec{y}\|} \right) \tag{3.17}$$

where $\vec{f}$ represents the filter, $\sup_{\vec{f}}$ denotes a supremum operator related to $\vec{f}$.

Given a set of real number S, β can be considered as the supremum of set S when β can meet the following two conditions simultaneously:

1) for all $x \in S$, $\beta \geq x$,

2) for each $e > 0$, $x > \beta - e$.

Therefore, it is possible to first solve $\vec{f}$ for each k, then select $\vec{f}$ for the maximum

D-norm. Equation (3.17) can be rewritten as:

$$\sup_{\vec{f}} D(\vec{y}) = \max_{k=1,2,\dots,N} \left(\sup_{\vec{f}} \frac{|y_k|}{\|\vec{y}\|} \right) \qquad (3.18)$$

Equation (3.18) can be differentiated with respective to the filter $\vec{f}$ to making derivative 0:

$$\frac{d}{d\vec{f}} \left(\frac{y_k}{\|\vec{y}\|} \right) = \vec{0} \qquad (3.19)$$

y_k in Equation (3.19) can be expressed as:

$$y_k = \sum_{l=1}^{L} f_l x_{k+L-l}, \quad k = 1, 2, \dots, N\text{-}L \qquad (3.20)$$

where L is the sample number.

The derivative of y_k can be expressed as:

$$\frac{dy_k}{df_l} = x_{k+L-l} \qquad (3.21)$$

$$\frac{d\|\vec{y}\|}{df_l} = \|\vec{y}\|^{-1} \sum_{k=1}^{N-L} y_k x_{k+L-1} \qquad (3.22)$$

Equation (3.19) can be expanded as:

$$\frac{d}{d\vec{f}} \left(\frac{y_k}{\|\vec{y}\|} \right) = \frac{x_{k+L-l}\|\vec{y}\| - y_k \|\vec{y}\|^{-1} \sum_{k=1}^{N-L} y_k x_{k+L-1}}{\|\vec{y}\|^2}$$

$$= x_{k+L-l}\|\vec{y}\|^{-1} - y_k \|\vec{y}\|^{-3} \begin{bmatrix} X_L \\ X_{L+1} \\ \vdots \\ X_N \end{bmatrix}^T \vec{y} = \vec{0} \qquad (3.23)$$

Converting Equation (3.23) to a matrix form for $l = 1, 2, \dots, L$, and making derivative 0

yields:

$$\frac{d}{d\vec{f}}\left(\frac{y_k}{\|\vec{y}\|}\right) = \|\vec{y}\|^{-1}\vec{M}_k - \|\vec{y}\|^{-3}y_k X_0\vec{y} = \vec{0} \tag{3.24}$$

$$\vec{M}_k = \begin{bmatrix} X_{k+L-1} \\ X_{k+L-1} \\ \vdots \\ X_k \end{bmatrix}, \quad X_0 = \begin{bmatrix} x_1 & x_2 & x_3 & \cdots & \cdots & x_N \\ 0 & x_1 & x_2 & \cdots & \cdots & x_{N-1} \\ 0 & 0 & x_1 & \cdots & \cdots & x_{N-2} \\ \vdots & \vdots & \vdots & \ddots & \cdots & x_{N-3} \\ 0 & 0 & 0 & \cdots & \cdots & x_{N-L+1} \end{bmatrix}$$

Since $\vec{y} = X_0^T\vec{f}$, Equation (3.24) can be represented as:

$$\frac{y_k}{\|\vec{y}\|^2}X_0 X_0^T\vec{f} = \vec{M}_k \tag{3.25}$$

where $(X_0 X_0^T)$ represents the un-normalized Toeplitz autocorrelation matrix of $\vec{x}$ with no assumed zero data.

Assume the $(X_0 X_0^T)^{-1}$ exist, Equation (3.25) can be rewritten as:

$$\frac{y_k}{\|\vec{y}\|^2}\vec{f} = (X_0 X_0^T)^{-1}\vec{M}_k \tag{3.26}$$

If $\vec{f}$ is a solution of Equation (3.26), then any multiple of $\vec{f}$ is also a solution. Therefore, the solution of the OMED filter can be represented as:

$$\vec{f} = (X_0 X_0^T)^{-1}\vec{M}_k \tag{3.27}$$

Changing the OMED filter length L from Equation (3.20) can provide different filter processing results. Figure 3.5 compares some processing results using the MED filter with different filter lengths. Figure 3.5(a) represents the simulated impulse signals; Figure 3.5(b) depicts the simulated impulsive signals with Gaussian white noise. Figures 3.5(c)(d)(e)(f) correspond to MED-filtered results for filter lengths of 20, 50, 80, and 110 respectively. The

shift of peak location from Figure 3.5 (d) is due to deconvolution filtering distortion. The results from Figures 3.5(c)-(f) indicate that with the adjustment of OMED filter length, the OMED filter can only recognize the single impulse with highest amplitude among the simulated multiple impulses.
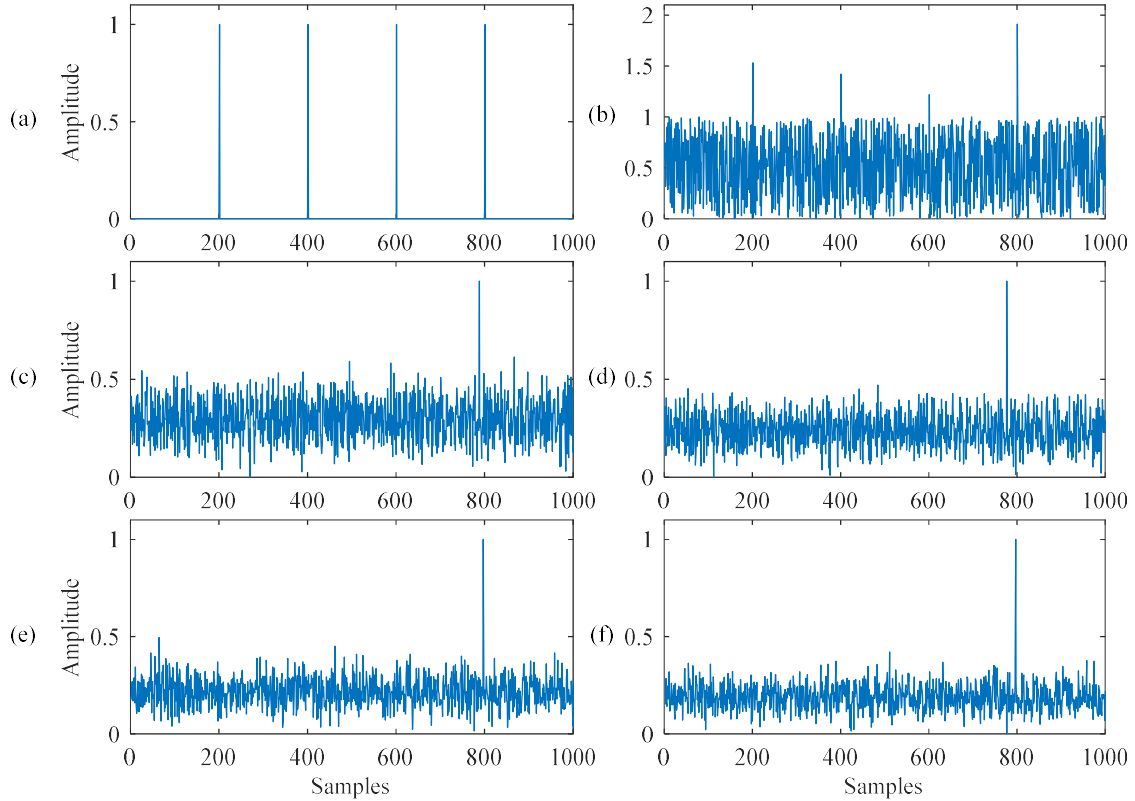
Figure 3.5: Comparison of OMED-filtered results at different filter lengths: (a) Simulated impulsive signal, (b) impulsive signal with noise, (c) OMED-filtered result with filter length $L = 20$, (d) OMED-filtered result with $L = 50$, (e) OMED-filtered result with $L = 80$, (f) OMED-filtered result $L = 110$.

3.4 MOMED Filtering

The Multipoint Optimal Minimum Entropy Deconvolution (MOMED) suggested in [74] is a deconvolution method that is used to recognize impulse-like features. Unlike the D-norm in OMED, the multi D-norm can be defined as:

$$D_M(\vec{y}, \vec{t}) = \frac{\vec{t}\vec{y}}{\|\vec{y}\|\|\vec{t}\|} \tag{3.28}$$

where $\vec{y}$ represents the vector form of a discrete-time series, $\vec{t}$ is the target vector that defines the location and weights of the target impulses, such as:

$$\vec{t} = \begin{bmatrix} 0 & 0 & 1 & 0 & 0 & 1 & 0 & 0 \end{bmatrix} \qquad (3.29)$$

Based on Equation (3.28), the MOMED can be undertaken by maximizing the $D_M(\vec{y},\vec{t})$:

$$\max D_M(\vec{y},\vec{t}) = \max_{\vec{f}} \frac{\vec{t}\vec{y}}{\|\vec{y}\|} \qquad (3.30)$$

By the chain rule, the derivative with filter coefficient $\vec{f}$ can be expressed as:

$$\frac{d}{d\vec{f}}\left(\frac{\vec{t}\vec{y}}{\|\vec{y}\|}\right) = \frac{d}{d\vec{f}}\frac{t_1 y_1}{\|\vec{y}\|} + \frac{d}{d\vec{f}}\frac{t_2 y_2}{\|\vec{y}\|} + \cdots + \frac{d}{d\vec{f}}\frac{t_{N-L} y_{N-L}}{\|\vec{y}\|} \qquad (3.31)$$

The derivatives for each of these terms are similar to those in the OMED in Equation (3.24), thus we can get:

$$\frac{d}{d\vec{f}}\left(\frac{t_k y_k}{\|\vec{y}\|}\right) = \|\vec{y}\|^{-1} t_k \vec{M}_k - \|\vec{y}\|^{-3} t_k y_k X_0 \vec{y} \qquad (3.32)$$

$$\vec{M}_k = \begin{bmatrix} X_{k+L-1} \\ X_{k+L-1} \\ \vdots \\ X_k \end{bmatrix}$$

Therefore, Equation (3.31) can rewrite as:

$$\frac{d}{d\vec{f}}\left(\frac{\vec{t}\vec{y}}{\|\vec{y}\|}\right) = \|\vec{y}\|^{-1}\left(t_1 \vec{M}_1 + t_2 \vec{M}_2 + \cdots + t_{N-L}\vec{M}_{N-L}\right) - \|\vec{y}\|^{-3}\vec{t}\vec{y}X_0\vec{y} \qquad (3.33)$$

By some manipulation related to $X_0\vec{t} = \left(t_1\vec{M}_1 + t_2\vec{M}_2 + \cdots + t_{N-L}\vec{M}_{N-L}\right)$, the extrema of Equation (3.33) can be calculated as:

$$\|y\|^{-1} X_0\vec{t} - \|\vec{y}\|^{-3}\vec{t}\vec{y}X_0\vec{y} = \vec{0} \qquad (3.34)$$

Assume $(X_0 X_0^T)^{-1}$ is not singular. Based on $\vec{y} = X_0^T \vec{f}$, Equation (3.34) can be rewritten as:

$$\frac{\vec{t}^T \vec{y}}{\|\vec{y}\|^2} \vec{f} = (X_0 X_0^T)^{-1} X_0 \vec{t} \tag{3.35}$$

Since a multiple of $\vec{f}$ are the solutions to Equation (3.35), $\vec{f} = (X_0 X_0^T)^{-1} X_0 \vec{t}$ can be considered as the solution of the MOMED filter [74].

3.5 MCKD Filtering

The Maximum Correlated Kurtosis Deconvolution (MCKD) proposed in [75] is an iterative deconvolution process to recognize impulses by using kurtosis. The correlated kurtosis of first-shift can be expressed as:

$$K_{c1}(T) = \frac{\sum_{n=1}^{N} (y_n y_{n-T})^2}{\left(\sum_{n=1}^{N} y_n^2\right)^2} \tag{3.36}$$

where T is the period of separation for these impulses.

The correlated kurtosis of M-shift can be determined by:

$$K_{CM}(T) = \frac{\sum_{n=1}^{N} \left(\prod_{m=0}^{M} y_{n-mT}\right)^2}{\left(\sum_{n=1}^{N} y_n^2\right)^{M+1}} \tag{3.37}$$

where M is the number of sequential impulses to be devonvloved.

The deconvolution of MCKD can be computed by:

$$\max_{\vec{f}} K_{CM}(T) = \max_{\vec{f}} \frac{\sum_{n=1}^{N} \left(\prod_{m=0}^{M} y_{n-mT}\right)^2}{\left(\sum_{n=1}^{N} y_n^2\right)^{M+1}} \tag{3.38}$$

An optimal $\vec{f}$ that can maximize Equation (3.38) can be considered as the solution of

the MCKD filter. The period can be calculated by:

$$T = \frac{f_s}{f_m} \tag{3.39}$$

where f_s is the sampling frequency in Hz and f_m is the fault characteristic frequency of the system (a rolling element bearing in this case) that generates impulsive signals.

On the other hand, from systematic research investigation, it is found that the period can be chosen as nT. Filter length L could be optimized based on signal properties.

3.6 Comprehensive Comparison

Figure 3.6 shows the comparison of simulated results using different denoising filters as discussed in this chapter. Figure 3.6(c)(d)(e)(f) depict the processing results using the related denoising filtering of the MED, OMED, AR, and MCKD, respectively. It is seen the MED filter (Figure 3.6(c)) and the OMED (Figure 3.6(d)) can recognize one signal impulse only at $t = 200$, and $t = 800$, respectively, which are due to the sensitiveness of optimization parameters. The AR filter (Figure 3.6(e)) can not clearly recognize all the simulated impulses. Figure 3.6(f) shows that the MCKD filter can recognize all the four impulses with the highest SNR, with proper inputs like period and filter length. The MCKD will be adopted as the denoising filter in this work, which will be discussed in Chapter 5.
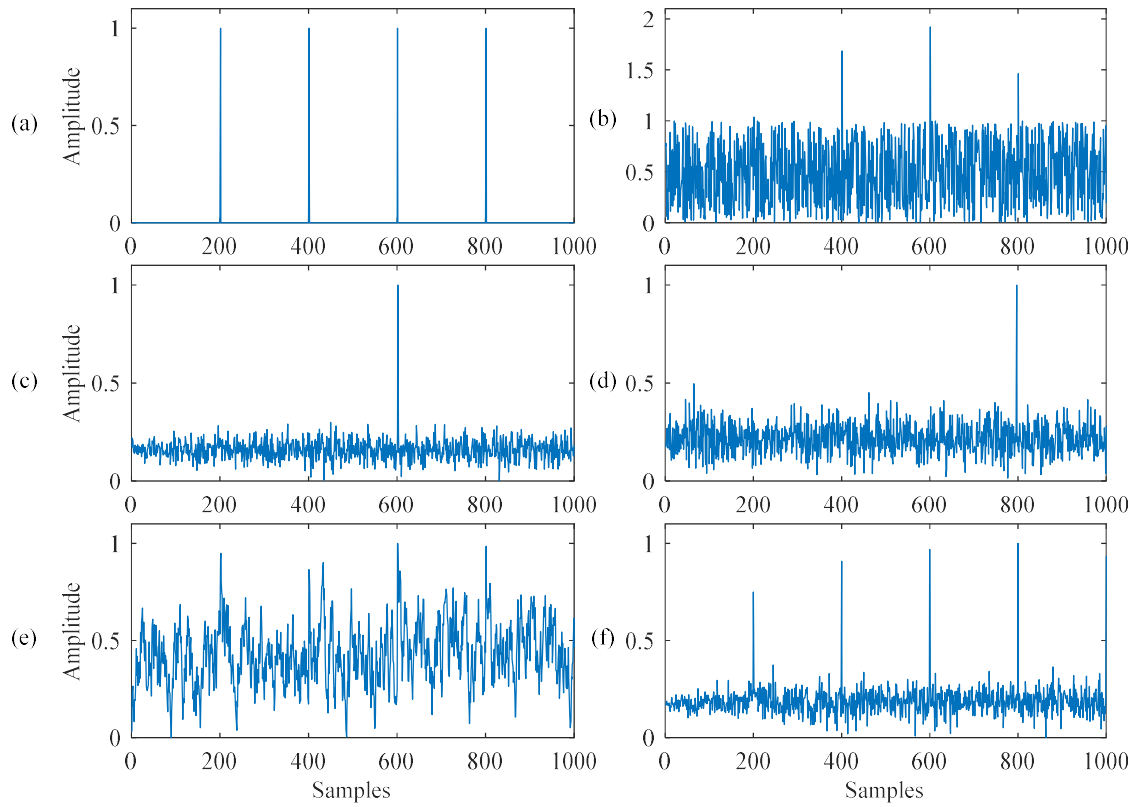
Figure 3.6: Comparison of filtered results corresponding to different filters: (a) Simulated impulsive signal, (b) impulsive signal with noise, (c) MED-filtered result, (d) OMED-filtered result, (e) AR-filtered result, (f) MCKD-filtered result.

Chapter 4

The Enhanced Teager-Huang Transform Technique for Bearing Fault Detection

The proposed enhanced Teager-Huang transform (eTHT) technique is developed for water pump health condition monitoring in the Bare Point Water Treatment Plant in Thunder Bay, by using a sensor network to monitor multiple bearings with the same specifications. It aims to reduce the signal processing workload for multiple sensors and improve the effectiveness of bearing fault detection.

The proposed eTHT technique is new in the following aspects:

1) A new strategy is proposed to construct a time-domain bearing fault characteristic relation function (CRF) with representative IMF for bearing fault diagnosis.

2) An average generalized Teager-Huang spectrum analysis method is introduced to extract the bearing fault features.

The proposed eTHT signal processing technique will take the following processing steps: 1) denoise filtering using MCKD method to enhance impulses features, 2) recognizing the representative IMF, and 3) computing the average generalized Teager-Kaiser (GTKA) spectrum for bearing fault detection.

Figure 4.1 illustrates the processing procedures in the proposed eTHT technique. The collected vibration signal is decomposed into a finite number of IMFs (e.g., 10 in this case). The similarity between the reference IMF and general IMFs is measured by using cross-correlation analysis, which is used to construct the CRF in the time domain. The details are discussed in the following sections.
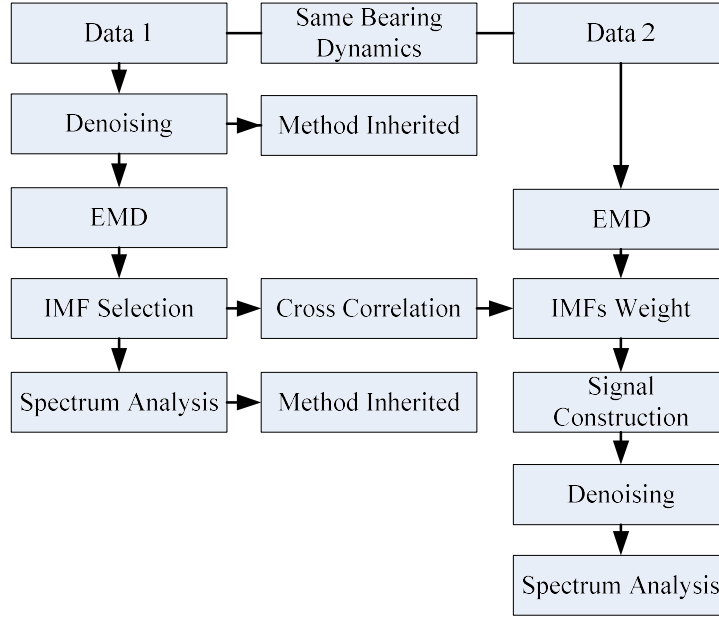
Figure 4.1: Procedures of the proposed eTHT technique.

4.1 The Hilbert Huang Transform

The Hilbert Huang transform (HHT) is an adaptive nonlinear and nonstationary signal processing method [48]. It consists of two processing stages: empirical mode decomposition (EMD) and IMF selection for spectrum analysis.

EMD is a process to decompose the original signal into a finite number of IMF by taking the following steps:

1) Identify the entire local extreme in the original data X_O.

2) Connect all the local maxima and local minima separately to form the upper and lower envelopes.

3) Calculate the mean of the upper and lower envelopes m_1.

4) Set the difference between the original data X_O and the mean m_1 as the first IMF, represented as,

$$IMF_1 = X_O - m_1 \qquad (4.1)$$

By repeating the aforementioned steps, the second IMF can be calculated as,

$$IMF_2 = IMF_1 - m_2 \qquad (4.2)$$

where m_2 is the mean value of both upper and lower envelopes of IMF_1.

Similarly, the kth IMF can be computed as,

$$IMF_k = IMF_{k-1} - m_k \qquad (4.3)$$

The IMFs must meet the following requirements:

1) For the whole data set, the number of zero-crossings and the number of extrema must either be equal or different at most by one.

2) At any point, the mean value of the envelopes must always be zero.

The IMF with the highest amplitude values of bearing fault characteristic frequency in the spectrum map will be considered as the reference IMF for CRF construction.

4.2 Reference IMF Selection

Figure 4.2 illustrates the first six IMFs from a bearing signal, which has an outrace fault. It is difficult to determine which IMF has the best characteristic features by directly viewing the graph properties from these subplots. Advanced analysis should be undertaken for signal processing and feature analysis for bearing fault detection.
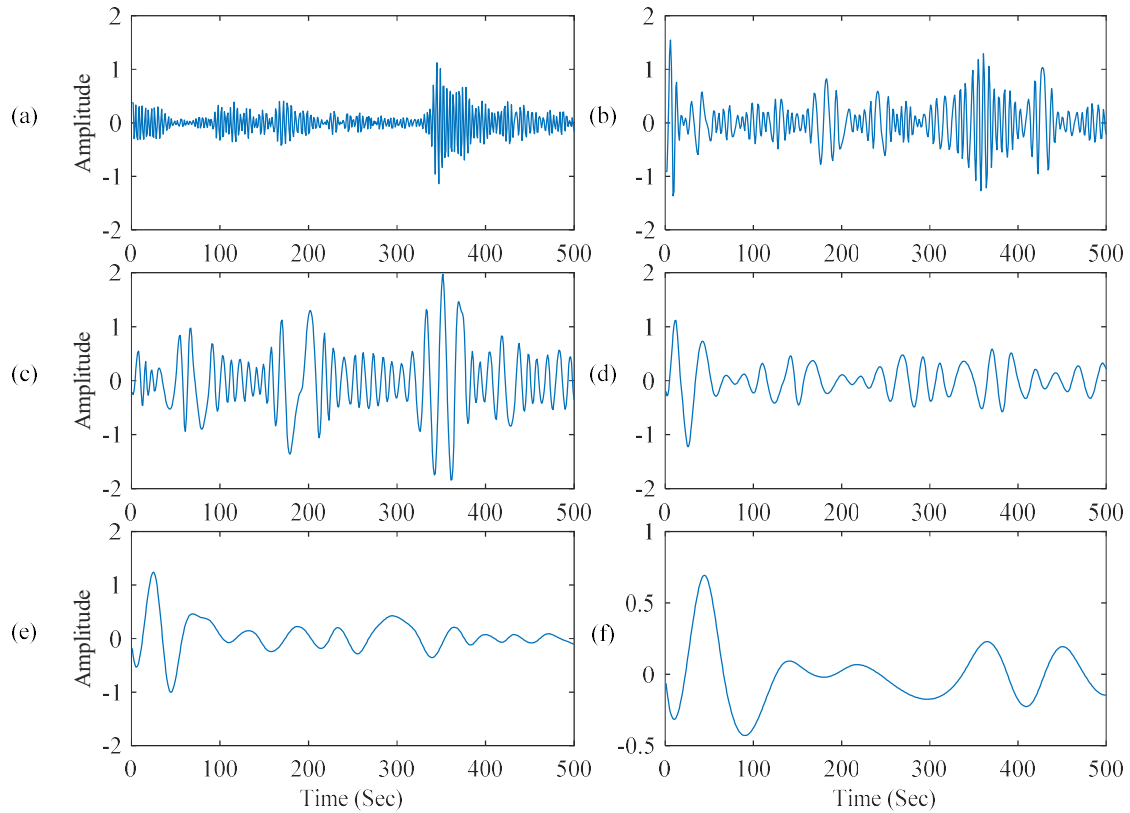
Figure 4.2: The first 6 IMFs of a vibration signal from a ball bearing with an outer race fault: (a) IMF1, (b) IMF2, (c) IMF3, (d) IMF4, (d) IMF5, (d) IMF6.

Figure 4.3 illustrates the Hilbert spectrum analysis results of IMF signals from Figure 4.2, corresponding to the first, second, third, fourth, fifth, and sixth IMF, respectively. Those black arrows in Figure 4.3 pointed out the peak of fault related features. It can be seen from Figure 4.3(a) that the first IMF can detect the first three harmonics of fault characteristic frequency. Figures 4.3(b) (e) (f) indicate that the second, fifth, and sixth IMF can detect the bearing characteristic frequency only. The spectrum analysis of the fourth IMF in Figure 4.3(d) can detect the second harmonics of the bearing fault characteristic frequency. On the other hand, the third IMF in Figures 4.3(c) cannot extract any fault-characteristic features. In this case, the first IMF will be selected as the reference IMF for cross-correlation analysis for bearing fault detection.
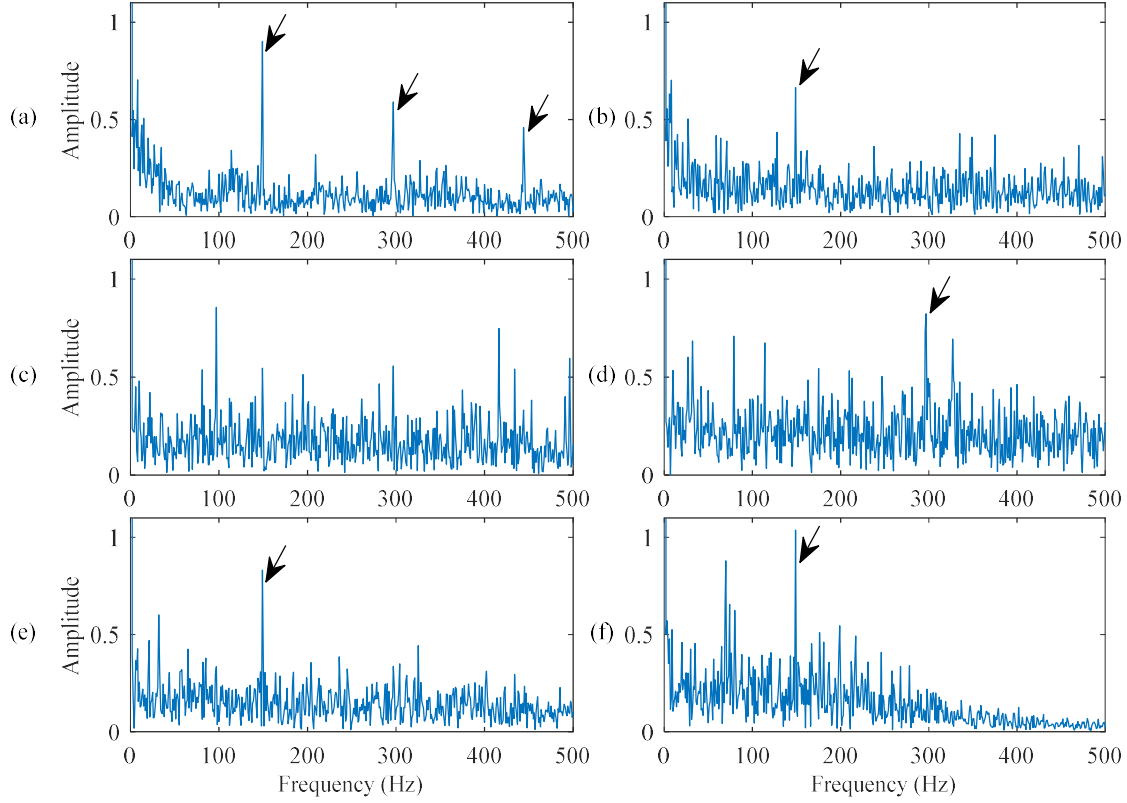
Figure 4.3: The first 6 spectrum maps of a outer race fault bearing signal's first 6IMF :(a) IMF1's spectrum analysis, (b) IMF2's spectrum analysis, (c) IMF3's spectrum analysis, (d) IMF4's spectrum analysis, (d) IMF5's spectrum analysis, (d) IMF6's spectrum analysis.

4.3 Cross-Correlation Analysis

Cross-correlation is a measurement between two or more sets of time series data to track the similarity properties of different time series. The cross-correlation of two random time series signals x_i and x_j can be measured by,

$$R_{xy} = \frac{r_{i,j}}{\sqrt{\sigma_i^2 \sigma_j^2}} \quad , \tag{4.4}$$

where σ_i and σ_j are the standard deviation values of x_i and x_j, respectively. The sample covariance $r_{i,j}$ can be determined by

$$r_{i,j} = \frac{1}{N} \sum_{t=1}^{N} [(x_i^t - E[x_i])(x_j^t - E[x_j])], \tag{4.5}$$

where $E[.]$ denotes the expectation operator.

Then Equation (4.4) can be rewritten as,

$$R_{ij} = \frac{\sum_{t-1}^{N} [(x_i^t - E[x_i])(x_j^t - E[x_j])]}{\sqrt{\sum_{t-1}^{N} (x_i^t - E[x_i])^2 \sum_{t-1}^{N} (x_j^t - E[x_j])^2}} \tag{4.6}$$

As discussed in section 4.2, the reference IMF can be found by spectrum analysis, which is then used for cross-correlation analysis with other IMFs. The IMF with the highest cross-correlation value can be selected for advanced spectrum analysis. Consider an example. The selected reference IMF is the second IMF from a signal collected from a bearing with ball fault and under heavy load condition. The IMFs are computed from a vibration signal collected from the same bearing with the same bearing dynamics, but under medium-load state. As illustrated in Figure 4.4, the third IMF has the highest representative feature related to ball fault in this case.
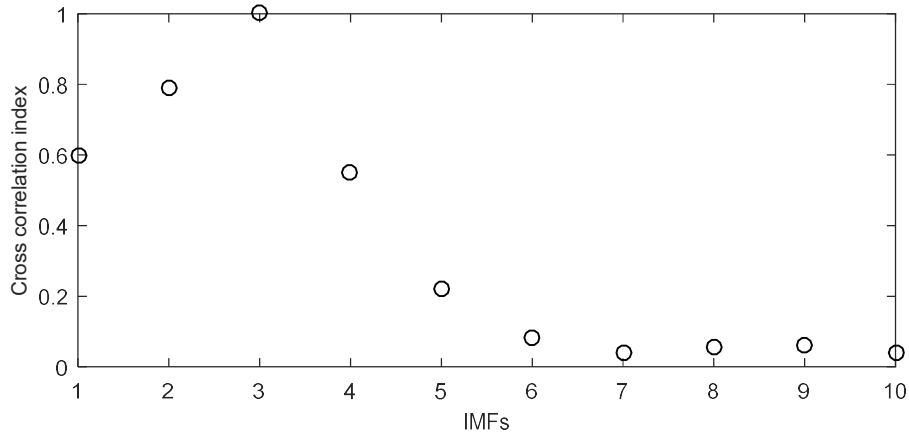
Figure 4.4: The cross-correlation values of the first 10 IMFs for a faulty bearing signal.

4.4 Characteristic Relation Function (CRF)

In this research, it is found that bearing fault features could be spread over multiple IMFs.

In Figure 4.4, for example, the dominant IMF is the third one or IMF_3, even though the first, second, and fourth IMFs also contain representative features to some extent. Or each of those IMFs can all recognize at least one of the characteristic frequencies on the spectral maps. From literature review in Chapter 1, EMD has a shortcoming that the same characteristic features are repeated in different IMFs [48]. Therefore, the objective of the proposed CRF is solving that problem in general EMD analysis. The CRF will be made by integrating multiple representatives IMFs with a weight factor to formulate a time-domain analytical signal for spectrum analysis.

As illustrated in Figure 4.5, the procedures of the CRF construction can be expressed as:

$$x(t) = \sum_{i=1}^{N} IMF_i \times w_i \tag{4.7}$$

where N is the total number of extracted IMFs, and w_i is the weight factor related to the cross-correlation index.
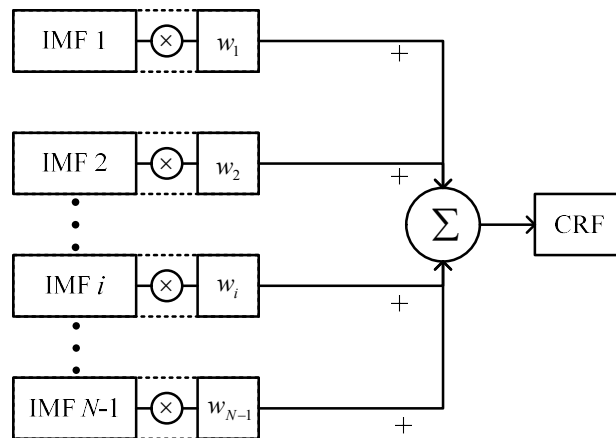
Figure 4.5: Illustration of the characteristic relation function construction.

4.5 Average Generalized Teager-Kaiser Spectrum Analysis

The GTKA analysis can remove some noise and enhance TK energy spectrum analysis. The GTKA is a combination of generalized TK processing and average spectrum analysis.

4.5.1 The Generalized Teager-Kaiser Processing

In signal processing, the TK analysis can be used to track the instantaneous energy of the signal [56], which is defined as,

$$\psi\{X_i[n]\} = X_i^2[n] - X_i[n-1]X_i[n+1],$$ (4.8)

where X_i is the *i*-th element of the targeted signals.

When the instantaneous energy experiences a sharp increase, the TK spectrum will generate an impulse to highlight that feature in the frequency domain. Therefore, the TK could be useful in detecting impulse features when an instantaneous frequency is detected. On the other hand, a misdiagnosis could occur due to TK's sensitivity to high-frequency noise. Therefore, generalized TK is suggested in this work to improve processing accuracy by reducing the noise sensitivity over a specific frequency bandwidth. The generalized TK can be defined as,

$$\psi_k\{X_i[n]\} = X_i^2[n] - X_i[n-k]X_i[n+k]$$ (4.9)

Unlike TK, a lag parameter *k* represents the distance between the samples. Consider the following simulated signal with amplitude modulation,

$$X_{AM}[n] = A\cos[2\pi f_c n](1 + k\cos[2\pi f_m n]) + N[n],$$ (4.10)

where $N[n]$ represent extra white noise, f_c is the carrier frequency, A represents the instantaneous amplitude, and f_m is the modulating frequency. The optimal lag parameter k can be determined by generating a spectrum where the amplitude of the modulating frequency is highlighted [28]. This optimal lag parameter k can be expressed as,

$$k = \arg\max_k \{P_{\psi k}(f = f_m)\},$$ (4.11)

where $P_{\psi k}$ is the frequency spectrum of generalized TK.

Based on the difference between modulation frequency f_m and carrier frequency f_c, the optimal lag K for GTK can be expressed as,

$$K = \begin{cases} \dfrac{f_s}{2f_m} & if \; f_m \leq f_c \\ \dfrac{f_s}{f_m} & if \; f_m > f_c \end{cases} \tag{4.12}$$

In electric current-based bearing fault detection, the modulation frequency f_m is higher than the carrier frequency f_c. However, in vibration-based bearing fault detection, the modulation frequency f_m is always lower than the carrier frequency f_c.

4.5.2 The Windowing Function

In signal processing, an appropriate window function can be used to smoothly draw a sampled signal down (or even to zero) over the starting and ending ends, so as to reduce spectral leakage. The leakage effect is the phenomenon of the smearing of power across a frequency spectrum that occurs when the signal being measured is not long enough or a rectangular window is used. Besides the default rectangular window, Hanning, Hamming, and Blackman are the commonly used window functions in signal processing [76]. For machinery vibration analysis, the Hanning window $X_n(n)$ and Hamming window $X_m(n)$ are widely used for leakage reduction, which are described as:

$$X_n(n) = \frac{1}{2}\left[1 - \cos\left(\frac{2\pi n}{M-1}\right)\right], \qquad 0 \leq n < M - 1 \tag{4.14}$$

$$X_m(n) = 0.54 + 0.46\cos\left[\left(\frac{2\pi}{M}\right)n\right], \qquad 0 \leq n < M - 1 \tag{4.15}$$

where M represents the signal (window) length.

Figure 4.6 demonstrates processing results using a rectangular window, a Hanning window and a Hamming window, for a vibration signal from a bearing with an outer race

fault. It is seen that compared with the use of a rectangle window (Figure 4.6(a)), the Hanning window (Figure 4.6(b)), can significantly reduce spectral leakage. On the other hand, the Hamming window (Figure 4.6(c)), has limited effect on spectral leakage reduction. By comparing the Hanning and Hamming window in Figure 4.6(d), it is clear that the Hanning window outperforms hamming window for leakage reduction. Therefore, the Hanning window will be used in this work.
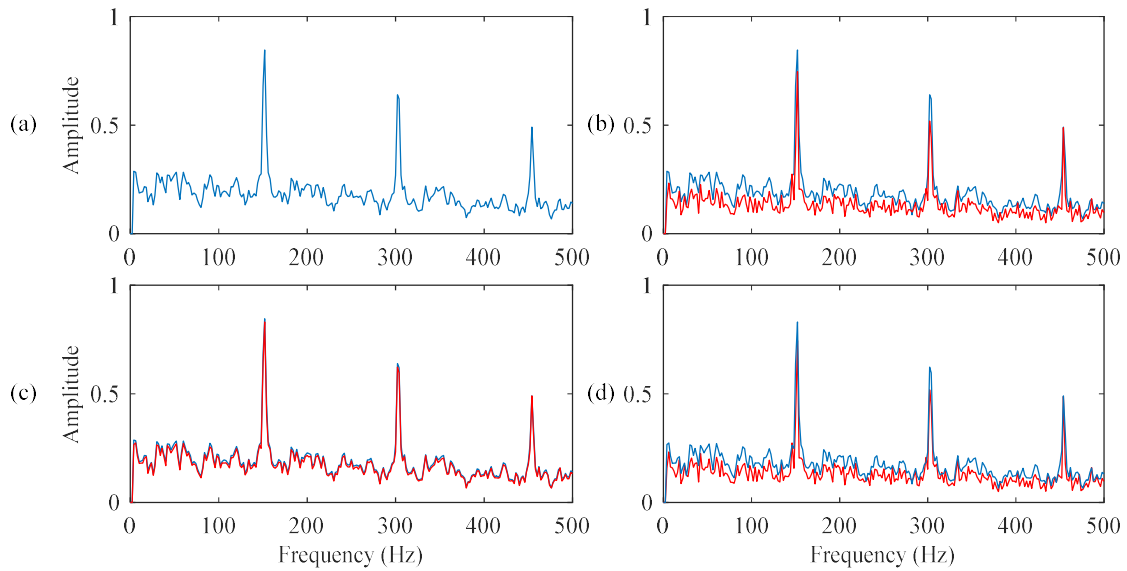
Figure 4.6: Comparison of spectral maps using a window function, subplot (a) rectangular window (blue line), (b) rectangular window (blue line) and a Hanning window (red line), (c) rectangular window (blue line) and a Hamming window (red line), (d) Hamming window (blue line) and a Hanning window (red line).

4.5.3 Spectrum Averaging

Spectrum averaging is a process to reduce noise variance by averaging the spectra [77]. It is to average the outputs of multiple spectral maps over a specific bandwidth, that make the random noise fluctuations in the spectra output decreased. If repeated time domain signals are not available, overlapping between adjacent segments of a long signal is also acceptable, as illustrated in Figure 4.7 with 50 percent overlap.
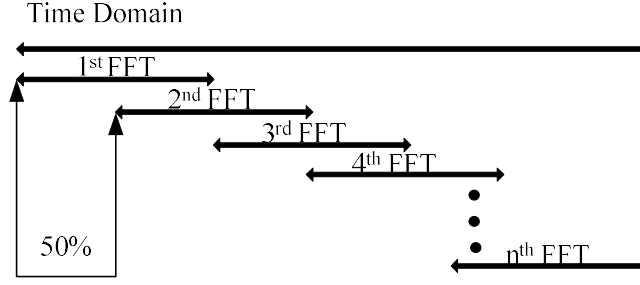
Figure 4.7: Illustration of spectrum averaging with a 50 percent overlap in the time signal.

Spectrum averaging can be undertaken by simply averaging some spectrums over the identical bandwidth such that,

$$S_1(n) = \frac{1}{P} \sum_{p=1}^{P} \left| F_p(n) \right| \tag{4.16}$$

where P is the total number of spectrums (i.e., the number of time signals) and $F_p(n)$ represents the p-th spectrum.

Because the real-world time-domain signals include constant phase information [78], to improve processing accuracy, coherent spectrum averaging will be conducted in this work, or the average is performed for both the real and the imaginary parts of spectral functions $F_p(n)$ such that,

$$S_2(n) = \frac{1}{P} \sum_{p=1}^{P} F_p(n)_{real} + j \frac{1}{P} \sum_{=1}^{P} F_p(n)_{imag} \tag{4.17}$$

The noise reduction effect can be measured by the SNR indicator, calculated by,

$$SNR = 20 \times \log_{10} \left(\frac{S_2}{F_N} \right), \tag{4.18}$$

where S_2 is the magnitude of coherent spectrum average as calculated from Eq. (4.17), and F_N is the magnitude of noise.

Figure 4.8 compares the results of a general spectral map (blue line) and a spectrum

average (red line) over six maps or signals (i.e., P = 6). The processing is for a vibration signal from a bearing with an outer race damage. The peak value of 153 Hz is the bearing fault characteristic frequency, and its harmonics. The average process can reduce the noise compared with the results without averaging, with a SNR of 8.695 dB versus 6.789 dB.
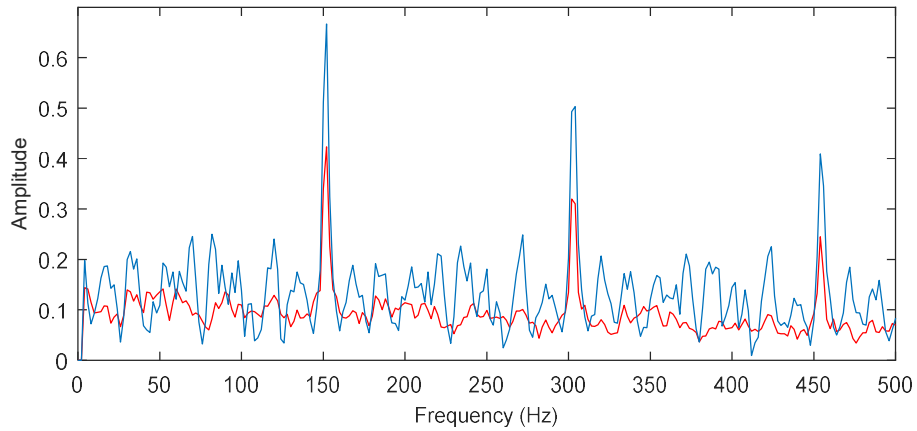
Figure 4.8: Comparison of the spectrum average (red line) and the original spectral map (blue line).

The effectiveness of the proposed eTHT technique will be examined experimentally in the next chapter with the comparison of the related techniques.

Chapter 5

Performance Verification

In this chapter, the effectiveness of the proposed eTHT technique will be verified experimentally. Its robustness of the proposed eTHT technique will be tested by using data sets from another experimental setup.

5.1 Experimental Setup

Figure 5.1 shows the experimental setup used in this test. The experiment setup consists of a 3hp induction motor with a speed range form 20 to 4200 rpm controlled by a variable frequency drive (VFD022B21A). A magnetic brake system is used as a dynamometer to simulate the loads. An optical sensor is used to provide a one-pulse-per-revolution signal for shaft speed measurement. An accelerometer (ICP-603C01) is mounted on the top of the tested bearing housing to measure the vibration signals along vertical axis. A flexible coupling is applied to remove the high-frequency vibration generated by the motor. The bearing (MB ER-10K) on the left-hand side of the housing is used for testing, which has following parameters:

Rolling elements $Z = 8$,

Rolling element diameter $d = 7.938$ mm,

Pitch diameter $D = 33.503$ mm,

Contact angle $\theta = 0$ degree.
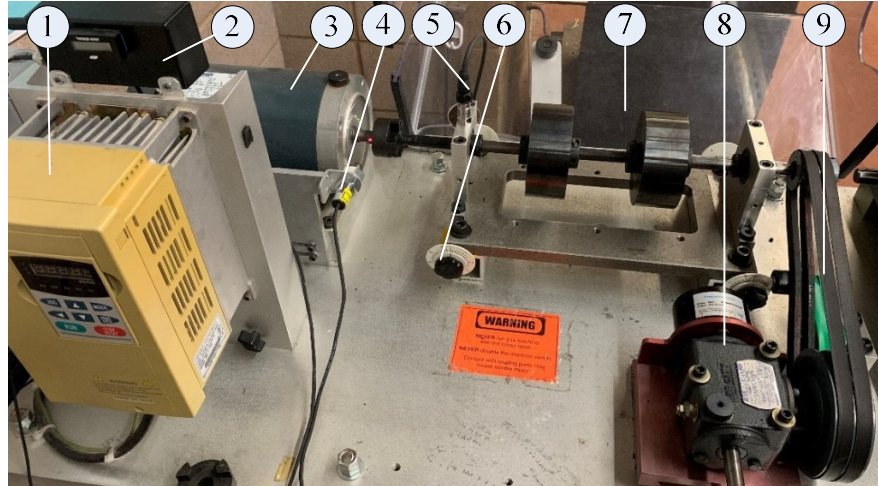
Figure 5.1: Experimental setup: (1) speed control; (2)encoder display; (3) motor; (4) optical encoder; (5) ICP accelerometer; (6) misalignment adjustor; (7) bearing housing; (8)variable load system; (9) belt drive.

5.2 Performance Evaluation

In this test, three bearing health conditions are considered for testing: Healthy bearing, bearing with outer race fault, and bearing with inner race fault. The performance of the proposed eTHT technique is represented as MCKD-GTKA. The following related techniques are used for comparison:

1) A well-accepted Hilbert spectrum transform (HHT) technique, denoted as MCKD-HHT, will be used to verify the effectiveness of the proposed eTHT technique.

2) The traditional Teager-Huang spectrum analysis, specified as MCKD-THT, will be applied to evaluate the efficiency of the proposed eTHT technique.

3) The proposed eTHT technique without using the MCKD denoising filter, denoted as GTKA, will be used to evaluate the performance of the denoising process.

All the techniques are implemented in MATLAB 2016. The selected sampling frequency is 20 kHz. A set of processing results with shaft speed of $f_r = 25$ Hz and load level of 1.2 Nm are used for illustration. Table 5.1 summarizes the characteristic frequencies in terms of

shaft speed f_r, calculated using Equations (1.1),(1.2),(1.3) for bearings with different health conditions.

Table 5.1: Bearing fault frequencies for the lab experiment setup

Bearing condition	Shaft Speed f_r
Healthy bearing	$f_H = f_r$
Outer-race fault	$f_{OD} = 3.03 \times f_r$
Inner-race fault	$f_{ID} = 4.93 \times f_r$

1) Healthy Bearing Monitoring

Firstly, a healthy bearing is tested, with the characteristic frequency of $f_H = 25\,\mathrm{Hz}$; Figure 5.2 illustrates the processing results using the related techniques. The optimal lag parameter $k = 400$ in Figures 5.2(c) and 5.2(d). A MCKD filter is applied with a length $L = 30$ and period $T = 800$ in Figure 5.2(a), 5.2(b), and 5.2(d). It is seen from in Figure 5.2(a) that the HHT can recognize the third harmonic of bearing bearing characteristic frequency in this case. MCKD-THT in Figure 5.2(b) is able to recognize the first five harmonics, but it has a lower SNR with comparison of Figure 5.2(d), or the GTKA technique is efficient to improve SNR. The comparison between Figure 5.2(c) and 5.2(d), shows that MCKD denoising filter can effectively lower random noise level, and improve SNR and faulty feature extraction ability.

Figure 5.2: Comparison of processing results of a bearing in healthy condition using the techniques of: (a) MCKD-HHT, (b) MCKD-THT, (c) GTKA, (d) MCKD-GTKA. Arrows specify characteristic frequency $f_H = 25$ Hz and its harmonics.

2) Outer-Race Bearing Fault Detection

In this test, a bearing with outer-race fault is installed and tested. With $f_r = 25$Hz, the characteristic frequency is $f_{OD} = 75.75$ Hz. Figure 5.3 illustrates the processing results using the related techniques. In the proposed GTKA technique, the optimal lag parameter $k = 132$. The MCKD filter has parameters of length $L = 100$ and period $T = 132$. In this case, all of the related techniques can recognize the occurrence of the bearing, because the features caused by outer race defect are periodic and are relatively easy to detect. On the other hand, the proposed MCK-GTKA technique in Figure 5.3(d) can still provide a higher SNR and resolution in features extraction.

Figure 5.3: Comparison of processing results of a bearing with outer-race fault using the techniques of: (a) MCKD-HHT, (b) MCKD-THT, (c) GTKA, (d) MCKD-GTKA. Arrows specify characteristic frequency $f_{od} = 75.75$ Hz, and its harmonics.

3) Inner-Race Fault Detection

Figure 5.4 shows the processing results for a bearing with an inner-race defect. In this case, with $f_r = 25$ Hz, the characteristic fault frequency is $f_{ID} = 123.25$ Hz. The optimal lag parameter $k = 81$. The MCKD filter parameters are $L = 100$ and $T = 264$. The MCKD-HHT in Figure 5.4(a) can recognize the first three harmonics of fault frequency, and performs better than MCKD-THT in Figure 5.4(b), due to the efficient TK analysis. Comparing Figure 5.4(b) and 5.4(d), it is seen that GTKA outperforms traditional THT in this case. The effectiveness of MCKD denoising is verified by comparing Figure 5.4(c) with 5.4(d); the proposed MCKD-GTKA method outperforms other methods in this case.
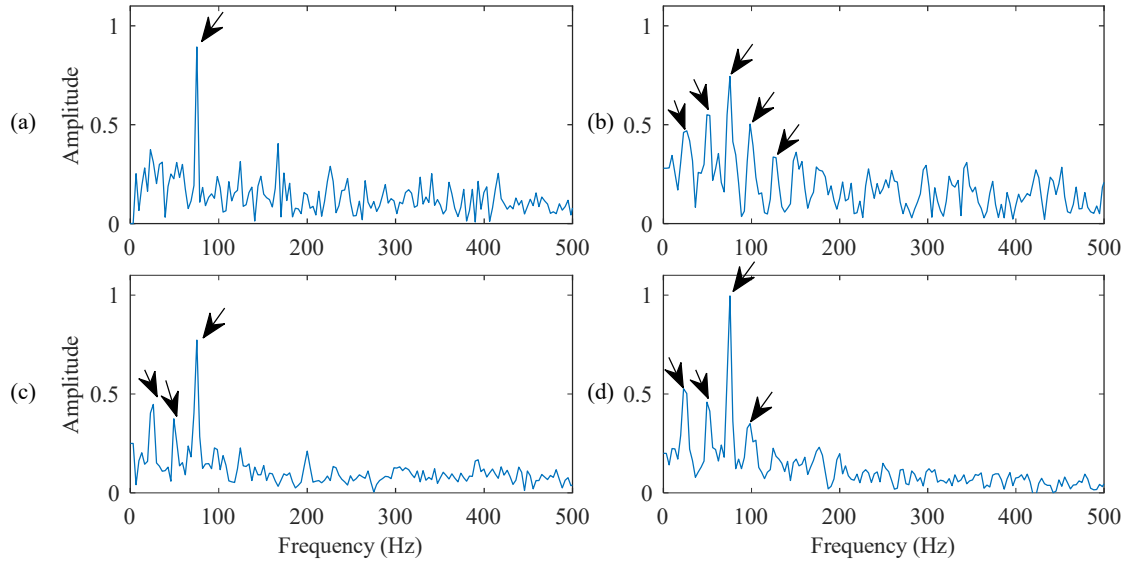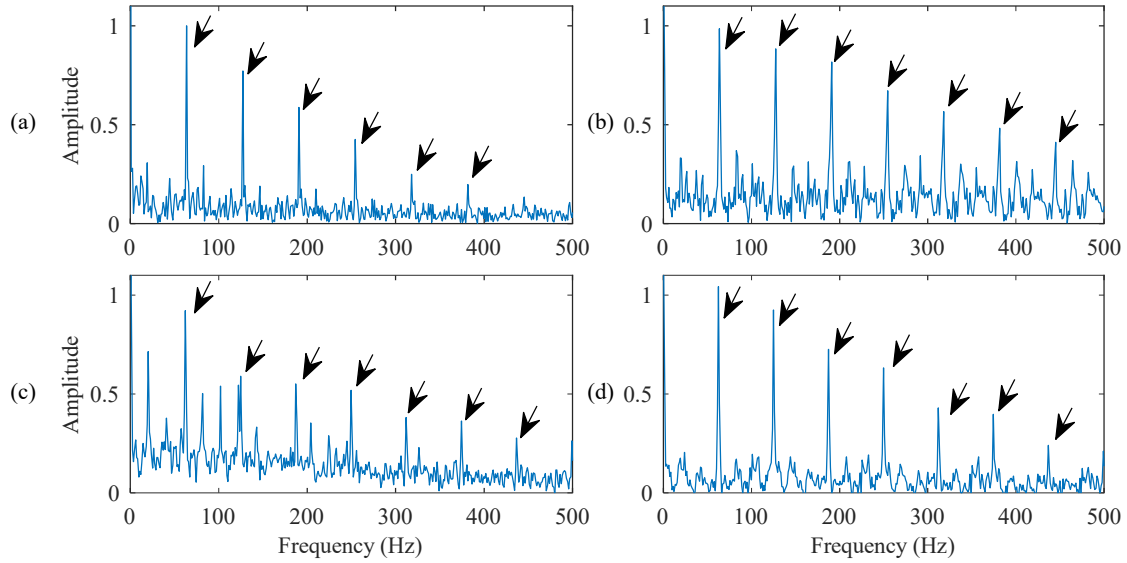
Figure 5.4: Comparison of processing results of a bearing with inner-race fault using the techniques of: (a) MCKD-HHT, (b) MCKD-THT, (c) GTKA, (d) MCKD-GTKA. Arrows specify characteristic frequency f_{id} = 123.35 Hz and its harmonics.

5.3 Performance Evaluation Using Data Sets Collected using Smart DAQ System

To further investigate the effectiveness of the proposed eTHT technique, another set of tests is undertaken with the same experimental setup but using the developed smart DAQ system. The sampling frequency of 20 kHz is used, with a medium load condition (i.e., 1.2 Nm). The shaft speed is f_r = 35 Hz. The processing results of the same techniques are listed below.

1) Healthy Bearing Condition Monitoring

Figure 5.5 shows the processing results for a healthy bearing testing. In this case, the characteristic frequency is f_H = 35 Hz. The optimal lag parameter k = 286. The MCKD filter parameters are L = 30 and T = 571. It is seen that the proposed MCKD-GTKA technique in Figure 5.5(d) provides the best processing results, compared with other related techniques. Comparing Figure 5.5(b) and 5.5(d), it can be seen that the GTKA has a better feature extraction capability than traditional THT method. The effectiveness of MCKD denoising process is verified by the comparison between the GTKA (Figure 5.5(c)) and the proposed

MCKD-GTKA.(Figure 5.5(d)).

Figure 5.5: Comparison of processing results of a bearing in healthy condition using the techniques of: (a) MCKD-HHT, (b) MCKD-THT, (c) GTKA, (d) MCKD-GTKA. f_H =35 Hz. Arrows specify characteristic frequency and its harmonics.

2) Outer-Race Fault Detection

Figure 5.6 shows the processing results for a bearing with outer-race fault. The characteristic frequency is $f_{OD} = 106.05\,\text{Hz}$ in this case. The optimal lag parameter is $k = 94$. The MCKD filter parameters are length $L = 100$ and period $T = 189$. Similarly, although each technique can predict the outer race defect, which is time-invariant in nature, the proposed eTHT technique in Figure 5.6(d) can provide better performance than other techniques with better resolution due to its efficient denoising filtering processing.
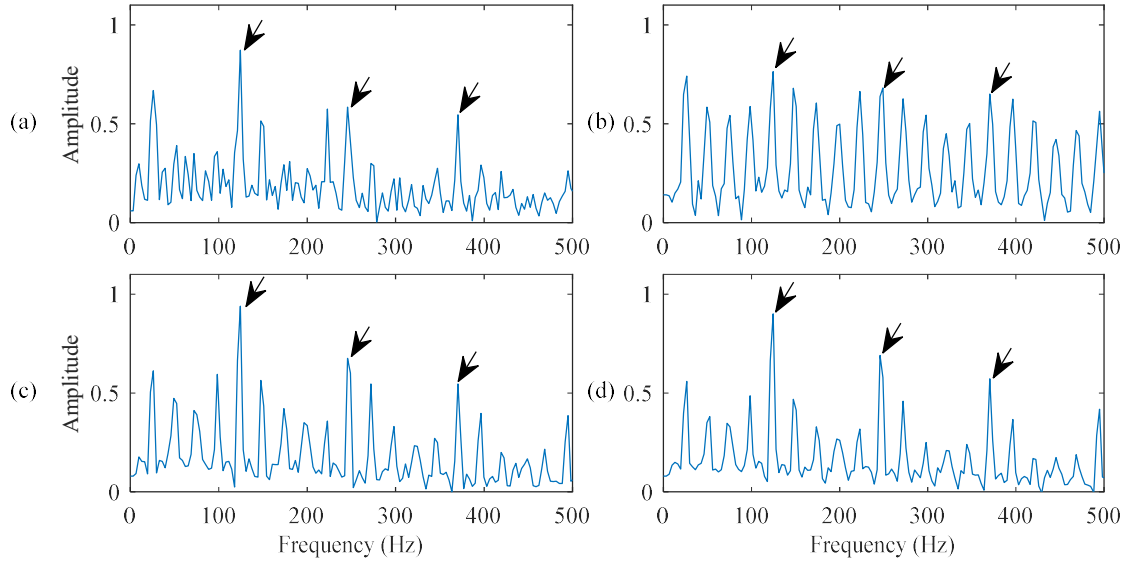
Figure 5.6: Comparison of processing results of a bearing with outer-race fault using the techniques of: (a) MCKD-HHT, (b) MCKD-THT, (c) GTKA, (d) MCKD-GTKA. f_{od} =106.05 Hz. Arrows specify characteristic frequency and its harmonics.

3) Inner-Race Fault Detection

Figure 5.7 shows the processing results for a bearing with an inner-race fault. The characteristic frequency is $f_{ID} = 172.55\,\text{Hz}$. The optimal lag parameter is $k = 58$, and MCKD filter parameters are $L = 100$ and $T = 116$. The MCKD-GTKA in Figure 5.7(d) outperforms MCKD-HHT in Figure 5.7(a) as well as MCKD-THT in Figure 5.7(b), due to its more efficient eHHT processing. The effectiveness of MCKD denoising process is proved by the comparison between Figure 5.7(c) and 5.7(d), which can improve the SNR and enhance fault detection accuracy.
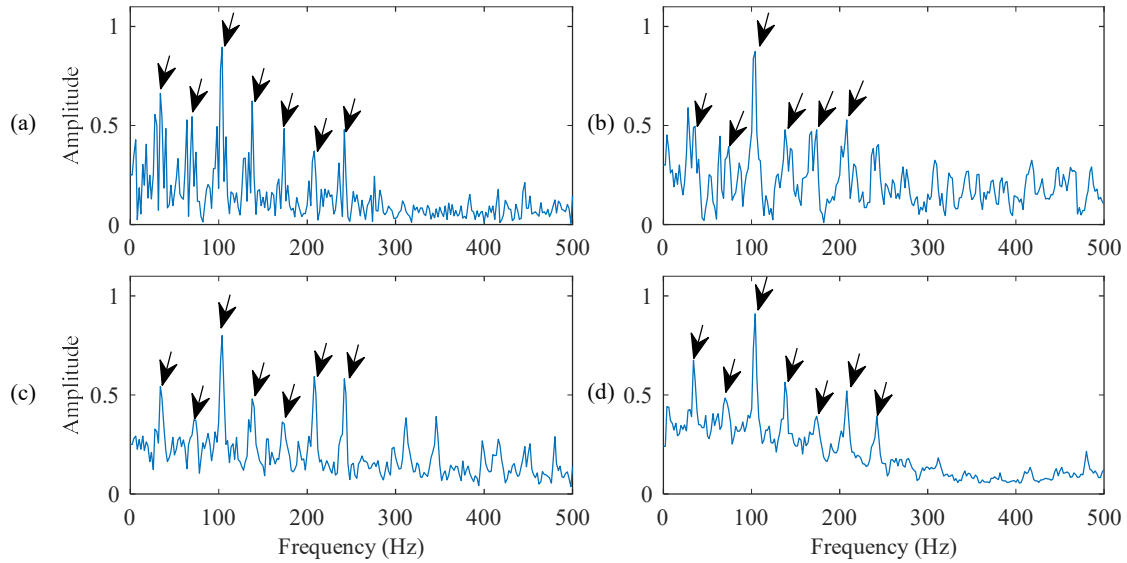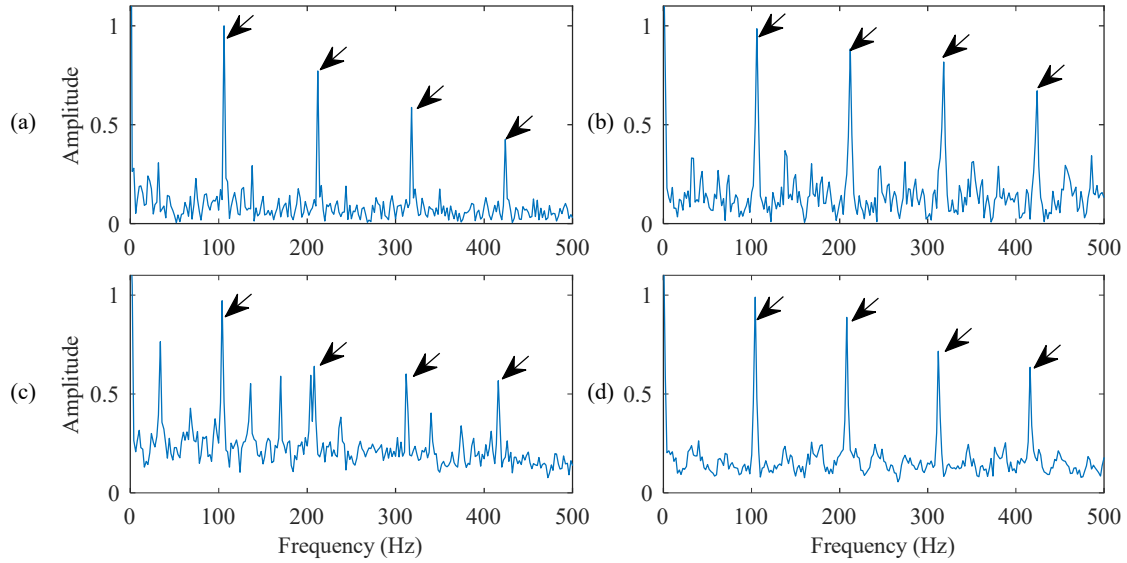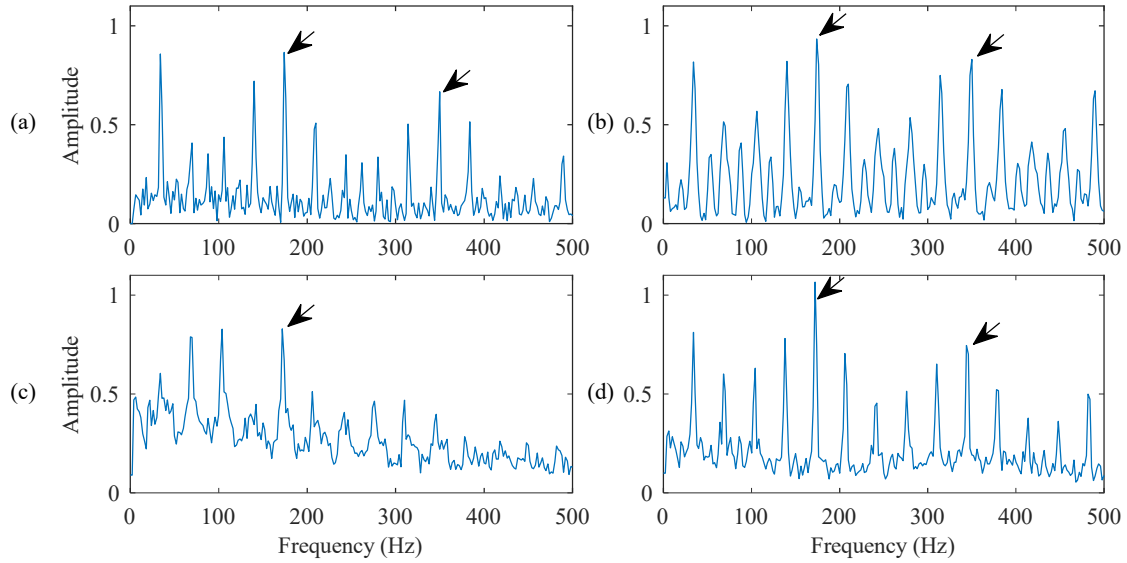
Figure 5.7: Comparison of processing results of a bearing with inner-race fault using the techniques of: (a) MCKD-HHT, (b) MCKD-THT, (c) GTKA, (d) MCKD-GTKA. f_{id} = 172.55 Hz Arrows specify characteristic frequency and its harmonics.

5.4 Robustness Testing

To investigate the robustness of the proposed eTHT technique under different load conditions, extra datasets are used from a different experiment setup at Case Western Reserve University (CWRU) Bearing Data Center [79]. As shown in Figure 5.8, the drive end bearing model is 6205-2RS JEM SKF (deep groove ball bearing from SKF) [80]. This bearing has the following parameters:

Rolling elements Z: 8,

Rolling element diameter d: 7.94 mm,

Pitch diameter D: 39.04 mm,

Contact angle θ: 0 degree.

The apparatus is driven by a 2-hp motor on the left. It has a torque transducer and a dynamometer for load. The vibration data was recorded for motor loads of 0 ~ 3 HP. A set of typical processing results with a motor speed ranges from 1797 rpm to 1720 rpm are used for evaluation.
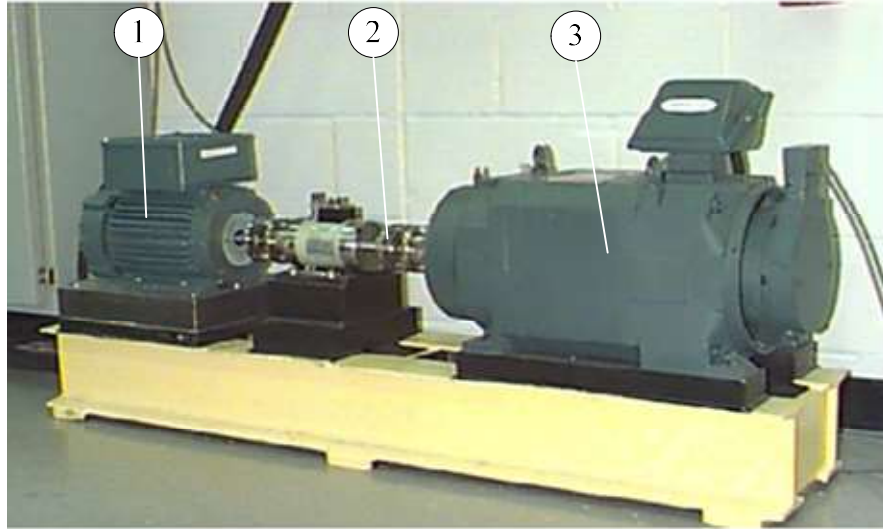
Figure 5.8: CWRU Bearing fault diagnosis experiment setup [79]: (1) drive motor, (2) tested bearing, (3) load motor.

Table 5.2 summarizes the characteristic frequencies in terms of shaft speed f_r for the tested bearing with different health conditions.

Table 5.2: Bearing fault frequencies for the online data center experiment setup

Bearing condition	Shaft Speed f_r
Healthy bearing	$f_H = f_r$
Outer-race fault	$f_{OD} = 3.5848 \times f_r$
Inner-race fault	$f_{ID} = 5.4152 \times f_r$
Rolling element fault	$f_{OD} = 4.7135 \times f_r$

In this experiment, four bearing health conditions are considered for testing: Healthy bearing, bearing with outer race fault, bearing with inner race fault, and bearing with rolling element defect. Three different bearing load conditions are considered for evaluation: no load (0 HP), medium-load (2 HP), and heavy-load (3 HP), where no load condition testing and diagnosis is important in repair and maintenance operations.

1) Healthy Bearing Condition Monitoring

Firstly, a healthy bearing is tested. Figure 5.9 shows the processing results under a medium load condition, with the characteristic frequency $f_H = 29.17$ Hz (the optimal lag $k = 205$, MCKD filter length $L = 30$ and period $T = 411$).

Figure 5.9: Processing results using the related techniques for a healthy bearing under medium load conditions: (a) MCKD-HHT, (b) MCKD-THT, (c) GTKA, (d) MCKD-GTKA. f_H=29.17 Hz. Arrows specify characteristic frequency and its harmonics.

From Figure 5.9(d), it is seen that the proposed eTHT technique can provide a little better diagnostic results than other related techniques due to its efficient MCKD denoising and GTKA spectrum analysis.

2) Outer-Race Fault Detection

In this testing, three load conditions are tested under similar (but a little different) speed conditions. Figure 5.10 shows the processing results for a bearing under no load condition, with the characteristic frequency of $f_{OD} = 107.36$ Hz (the optimal lag $k = 56$, MCKD filter length $L = 100$ and period $T = 113$). Figure 5.11 shows the processing results under a medium load condition, with the characteristic frequency is $f_{OD} = 104.56$ Hz (the optimal lag $k = 57$, MCKD filter length $L = 100$ and period $T = 115$). Figure 5.12 shows the processing

results under a heavy load condition, with the characteristic frequency being $f_{OD} = 103.36$ Hz (the optimal lag $k = 58$, MCKD filter length $L = 100$ and period $T = 116$).
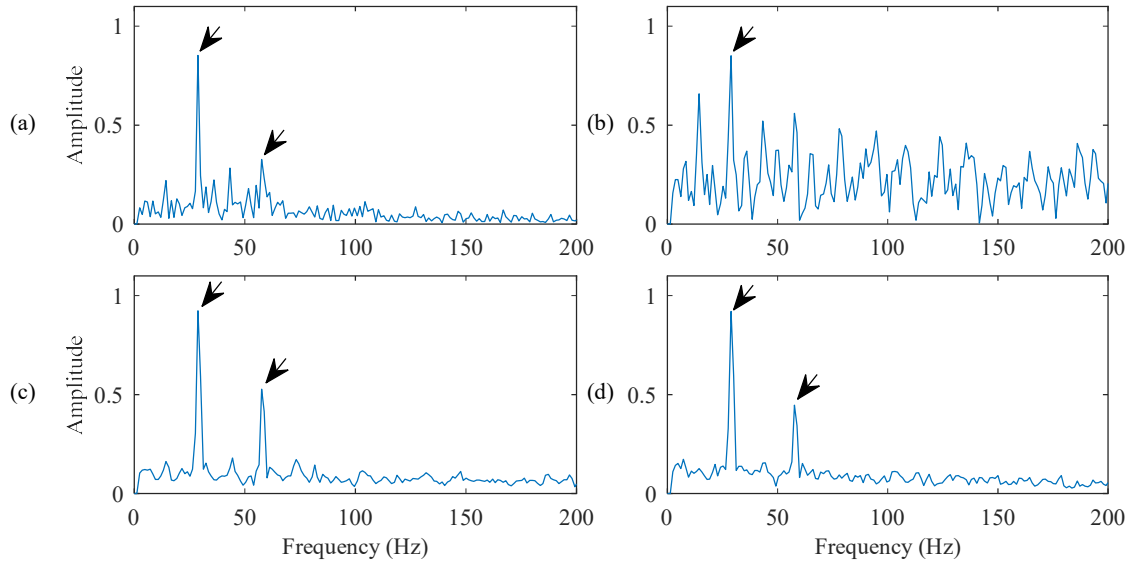

Figure 5.10: Processing results using the related techniques for a bearing with an outer race fault under no load conditions: (a) MCKD-HHT, (b) MCKD-THT, (c) GTKA, (d) MCKD-GTKA. f_{od}=107.36 Hz. Arrows specify characteristic frequency and its harmonics.

Figure 5.11: Processing results using the related techniques for a bearing with an outer race fault under medium load conditions: (a) MCKD-HHT, (b) MCKD-THT, (c) GTKA, (d) MCKD-GTKA. f_{od} =103.36 Hz. Arrows specify characteristic frequency and its harmonics.

Figure 5.12: Processing results using the related techniques for a bearing with an outer race fault under heavy load conditions: (a) MCKD-HHT, (b) MCKD-THT, (c) GTKA, (d) MCKD-GTKA. f_{od} =107.36 Hz. Arrows specify characteristic frequency and its harmonics.

From the above results corresponding to a bearing with an outer race damage under different load conditions, it is seen that although it is relatively easy to predict bearing fault if defect occurs on the fixed outer race, as the fault features are periodic and time-invariant, the proposed eTHT technique can provide better performance under different load conditions, with a better resolution due to its efficient GTKA processing.

3) Inner-Race Fault Detection

Figure 5.13 shows the processing results for the tested bearing with an inner race defect, under no load condition with the characteristic frequency being $f_{ID} = 162.19$ Hz (the optimal lag $k = 37$, MCKD filter length $L = 100$ and period $T = 74$). Figure 5.14 shows the processing results for the tested bearing with an inner race defect, under medium condition with the characteristic frequency of $f_{ID} = 157.94$Hz (the optimal lag $k = 38$, MCKD filter length $L = 100$ and period $T = 76$). Figure 5.15 shows the processing results for the tested bearing with an inner race defect, under heavy condition with the characteristic frequency of $f_{ID} = 156.14$ Hz (the optimal lag $k = 38$, MCKD filter length $L = 100$ and period $T = 77$).
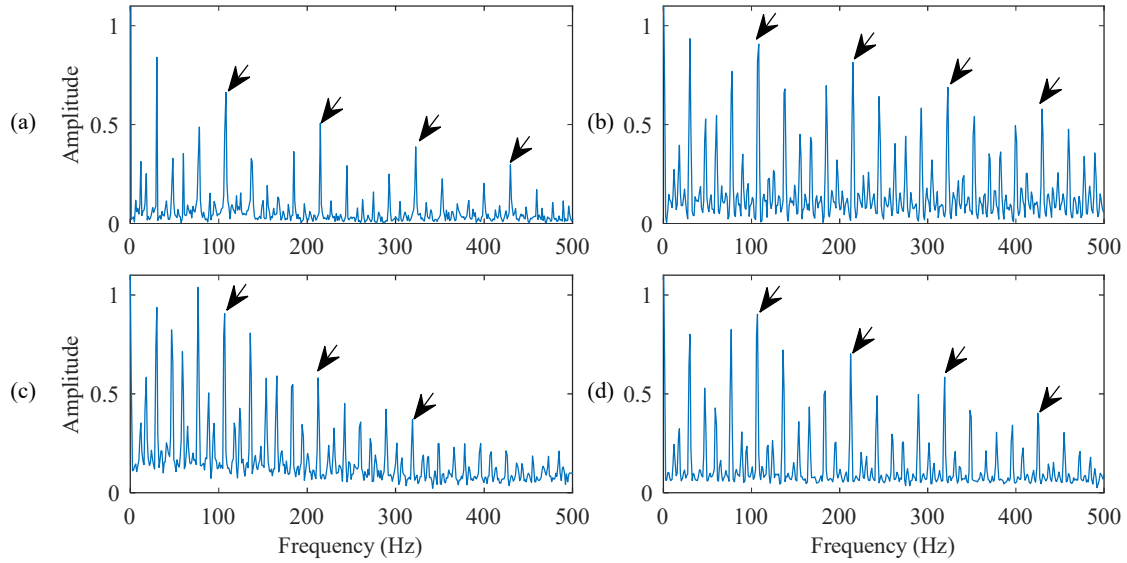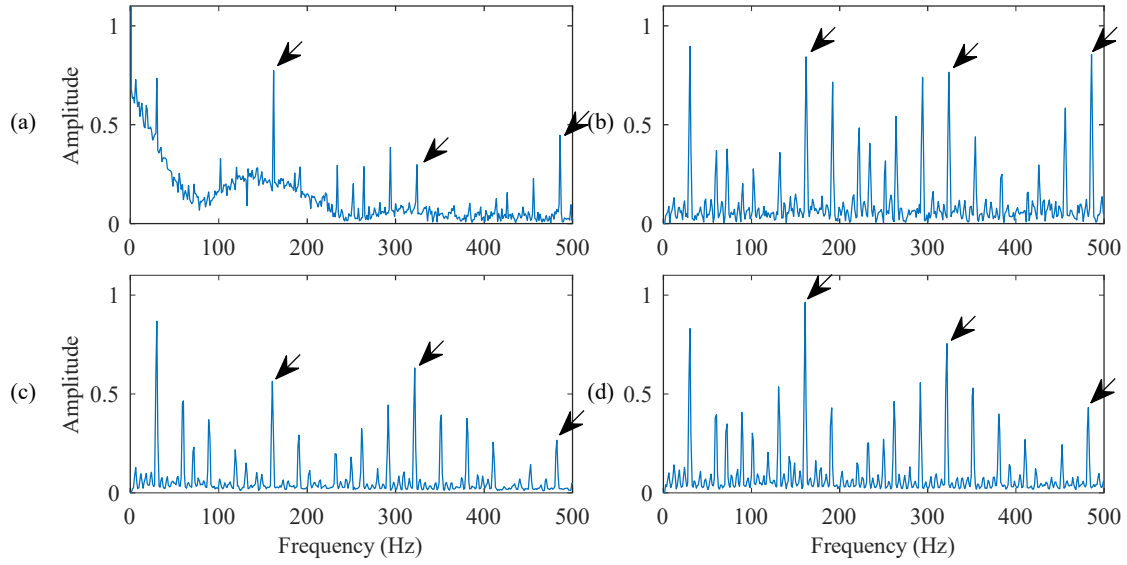
Figure 5.13: Processing results using the related techniques for a bearing with an inner race fault under no load conditions: (a) MCKD-HHT, (b) MCKD-THT, (c) GTKA, d) MCKD-GTKA. f_{id} = 162.19 Hz. Arrows specify characteristic frequency and its harmonics.
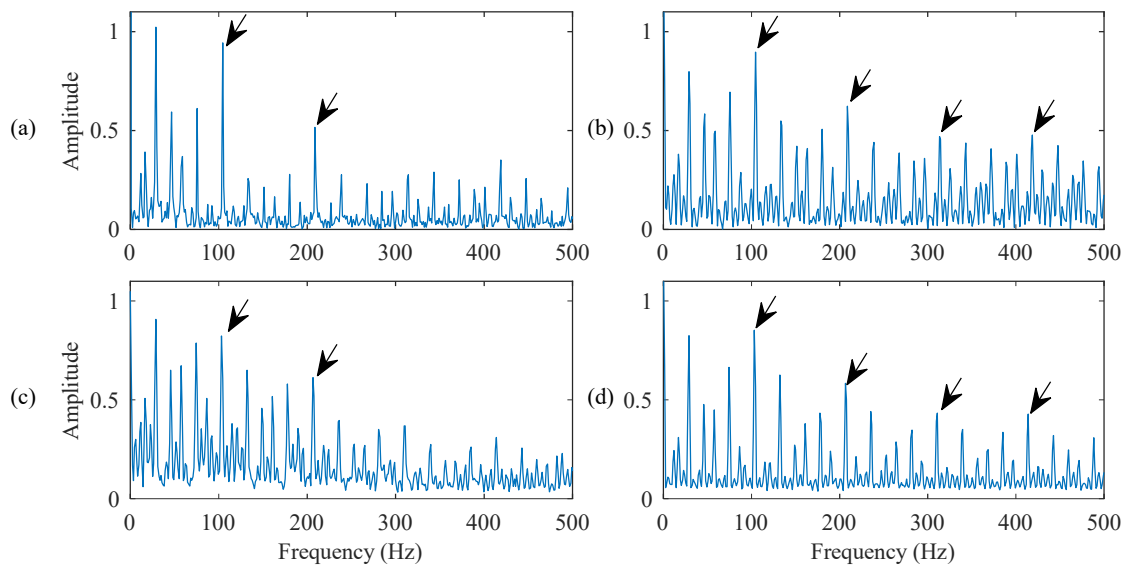

Figure 5.14: Processing results using the related techniques for a bearing with an inner race fault under medium load conditions: (a) MCKD-HHT, (b) MCKD-THT, (c) GTKA, (d) MCKD-GTKA. f_{id} = 157.94 Hz. Arrows specify characteristic frequency and its harmonics.
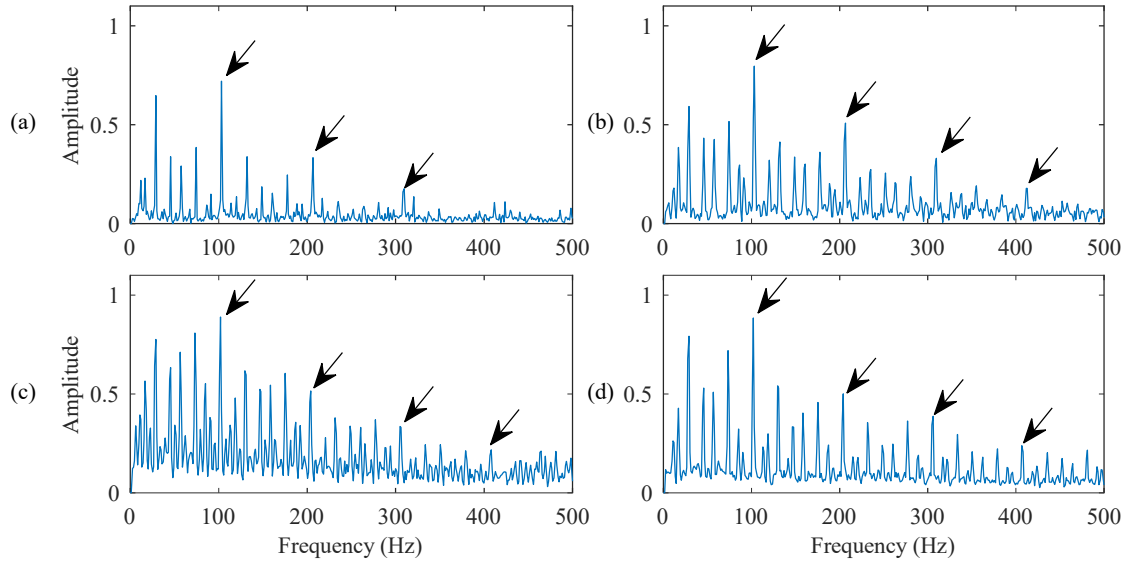
Figure 5.15: Processing results using the related techniques for a bearing with an inner race fault under heavy load conditions: (a) MCKD-HHT, (b) MCKD-THT, (c) GTKA, (d) MCKD-GTKA. f_{id} = 156.14 Hz. Arrows specify characteristic frequency and its harmonics.

From the above results corresponding to a bearing with inner race damage under different load conditions, it is seen that all the spectrums can show several harmonic peaks of the inner race fault frequency. In addition, the inner race fault defects generate a sideband frequencies spaced below and above the bearing defect frequencies. Usually, these sidebands will be spaced at around 1 rpm and the amplitudes of the specified defect frequencies are rarely very high. This problem is well addressed by the proposed eTHT technique that it can provide better performance under different load conditions, with a higher SNR and higher amplitudes of the specified defect frequencies. Therefore, the proposed eTHT technique outperforms other technique for inner race fault detection under different load conditions.

4) Rolling Element Fault Detection

Next a bearing with a simulated defect (with a dimension of 0.021 inches) in a rolling element is tested. Figure 5.16 shows the processing results using the related technique under no load condition with the characteristic frequency $f_{RD} = 141.17\,\text{Hz}$ (lag parameter k = 42, MCKD filter length L =100 and period T = 85). Figure 5.17 shows the processing results for the tested bearing under medium load condition, with the characteristic frequency

$f_{RD} = 137.48$Hz (lag $k = 44$, MCKD, $L = 100$, $T = 87$). Figure 5.18 shows the processing

results for the tested bearing under heavy load condition, with the characteristic frequency

$f_{RD} = 135.9$Hz (with the optimal lag $k = 44$, MCKD filter $L = 100$ and period $T = 788$).
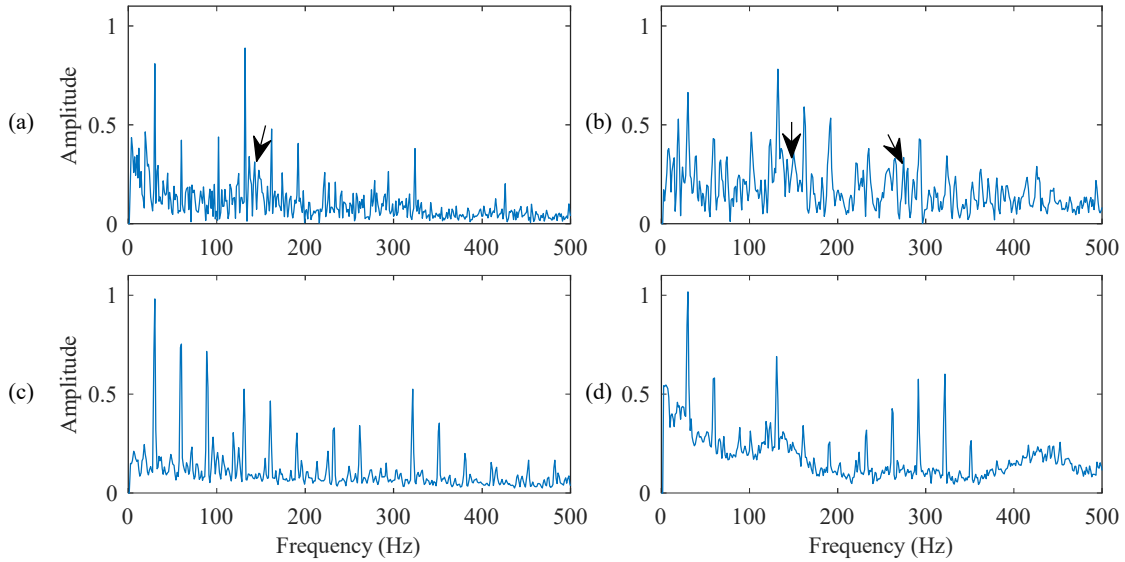
Figure 5.16: Processing results using the related techniques for a bearing with a ball fault under no load conditions: (a) MCKD-HHT, (b) MCKD-THT, (c) GTKA, (d) MCKD-GTKA. $f_{rd} = 141.17$ Hz. Arrows specify characteristic frequency and its harmonics.
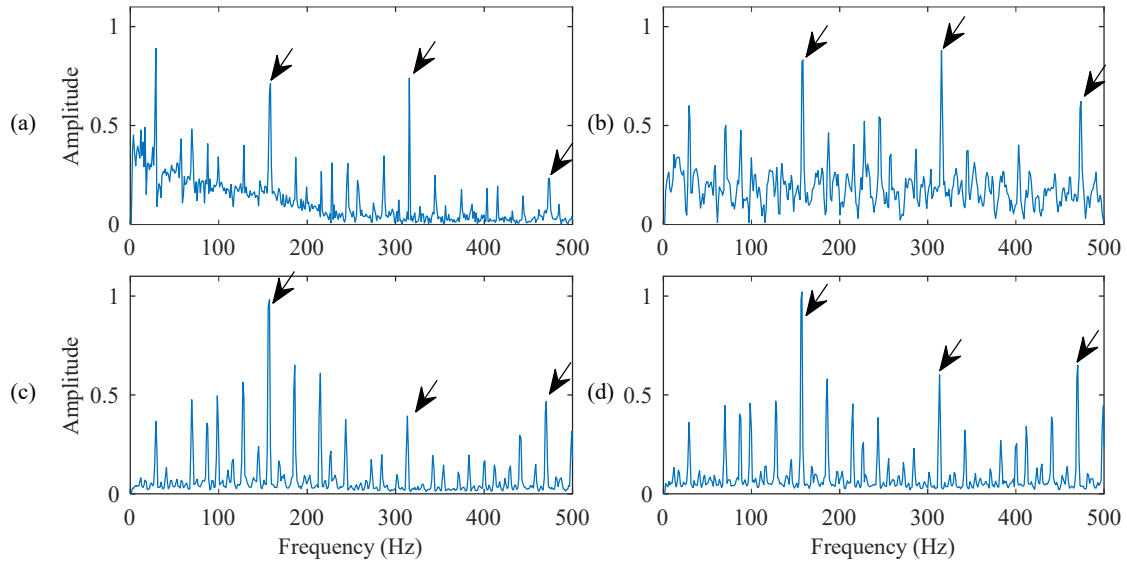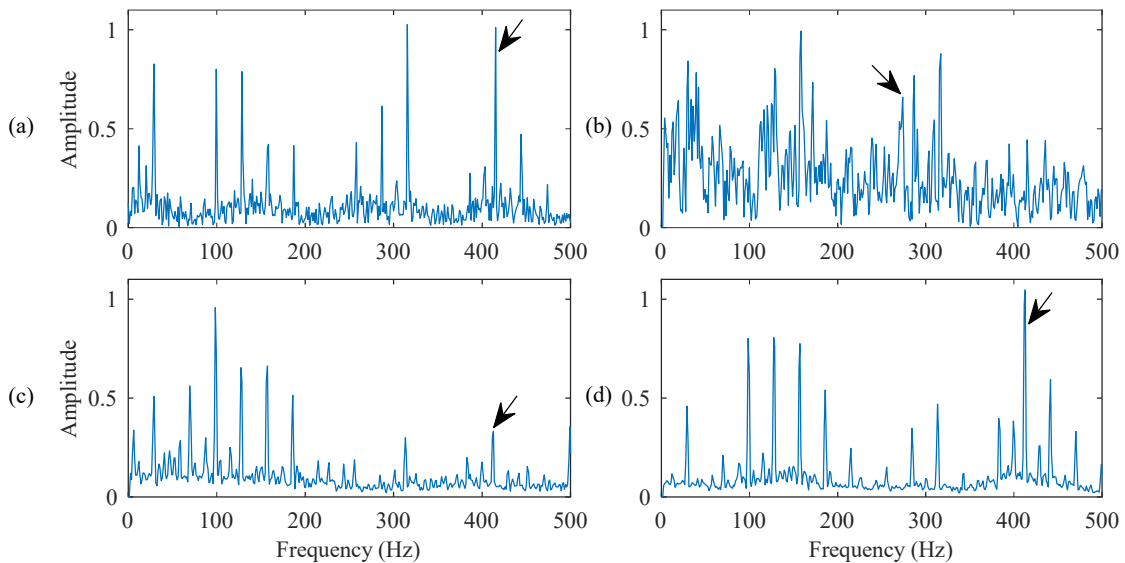

Figure 5.17: Processing results using the related techniques for a bearing with a ball fault under medium load conditions: (a) MCKD-HHT, (b) MCKD-THT, (c) GTKA, (d) MCKD-GTKA. $f_{rd} = 137.48$ Hz. Arrows specify characteristic frequency and its harmonics.
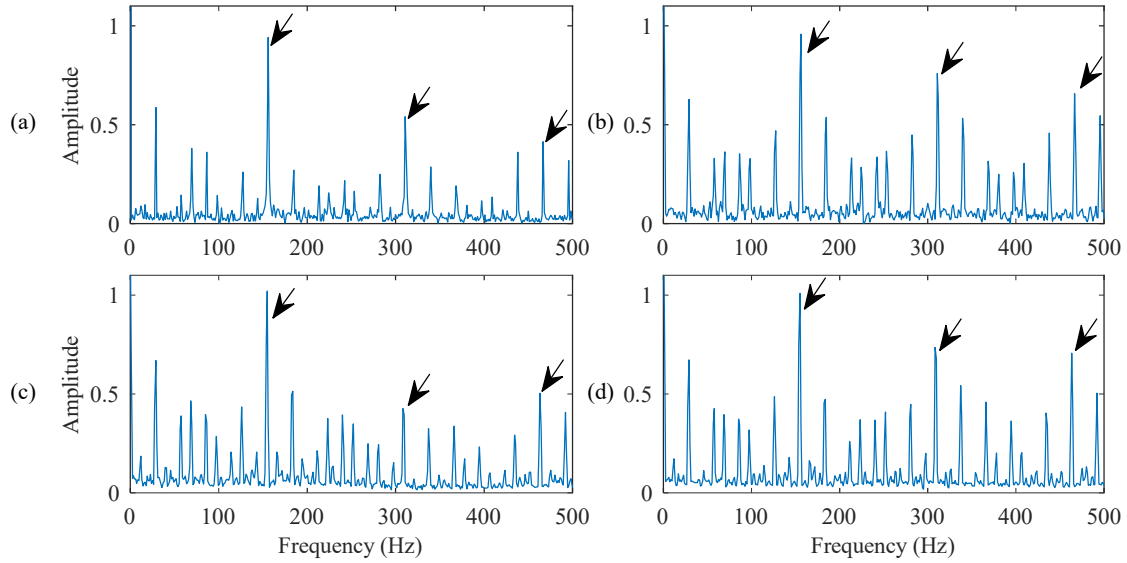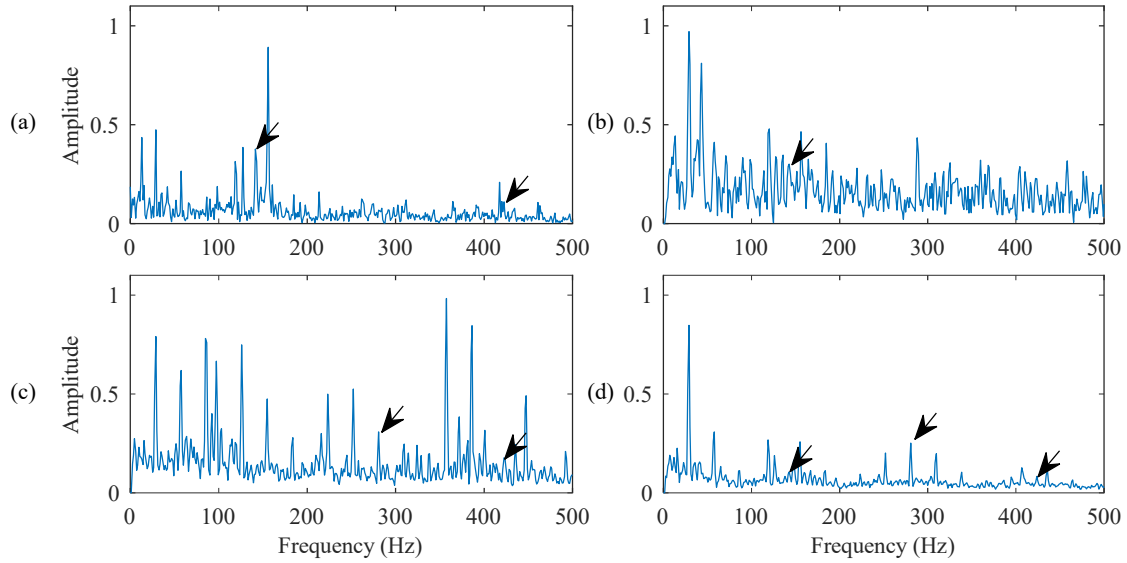
Figure 5.18: Processing results using the related techniques for a bearing with ball fault under heavy load conditions: (a) MCKD-HHT, (b) MCKD-THT, (c) GTKA, (d) MCKD-GTKA. f_{rd} = 135.9 Hz. Arrows specify characteristic frequency and its harmonics.

From the above results corresponding to a bearing with ball element fault damage under different load conditions, it is seen that it is difficult for these methods to detect ball element fault. Similar to inner race, rolling element bearing defects will be accompanied by sideband frequencies spaced below and above the bearing defect frequencies. The amplitudes of the specified defect frequencies are very low which make it difficult for features extraction. However, it is found in Figure 5.17 that the proposed eTHT technique can successfully detect the third harmonic of defect frequency due to the effectiveness of proposed GTKA method.

Chapter 6

Conclusions and Future Work

6.1 Conclusions

Rolling element bearings are commonly used in rotating machinery, while most machinery imperfections are related to bearing defects. reliable techniques and monitoring system for bearing fault diagnostics are critically needed in industries, that can help recognize a bearing defect at its early stage to prevent the machinery performance degradation and malfunction. Although many signal processing techniques have been proposed in the literature for bearing fault detection, each technique has its own strength and limitation and can be used for bearing fault detection under specific dynamics conditions. Reliable real-time bearing health condition monitoring is still a challenge task in this research and development field. The first reason is related to DAQ limitations, and second reason is related to the robustness of bearing fault detections. The objective of this work is to develop a new bearing health condition monitoring system for more reliable bearing fault detection in real-time.

Firstly, a ZigBee wireless DAQ system has been developed for data acquisition. New programs have been developed for auto DAQ and power-saving. An interface program has been improved to properly implement and control data pre-processing and other DAQ functions. The system with two sensor nodes has been developed with improved function execution timing and system.

Secondly, a WiFi DAQ system has been studied and improved. The capability of the ESP32-S2 has been investigated and used in this work. An SPI communication protocol has been programmed and implemented.

Thirdly, a new enhanced Teager-Huang transform technique, eTHT in short, has been proposed for bearing fault detection. The eTHT takes several processing procedures. First, the EMD is applied to decompose the denoised the signal into several IMFs with different frequency components. Second, a reference IMF is selected for each bearing health

conditions by applying spectrum analysis. Third, a constructed characteristic relation function with the reference IMF is proposed for fault features composition. Then a denoising filter is applied to improve the signal to noise ratio. The spectrum average is used to reduce the random noise and extract the characteristic fault features for bearing fault detection.

The effectiveness of the proposed eTHT technique is verified by comparing its performance with other related techniques. The test results show that MCKD can properly denoise the signal and highlight the fault-related signatures for bearing health condition monitoring. The eTHT technique outperforms other related techniques by effectively improving the signal-to-noise ratio and highlighting the fault-related signatures. The robustness of the proposed eTHT technique is verified by tests using datasets from a different test apparatus (online data). The results show that the proposed eTHT technique is an efficient signal processing technique for bearing fault detection. The proposed eTHT technique has potential to be used for bearing fault detection in real industrial monitoring applications.

6.2 Future Work

The following advanced R&D work will be undertaken in the future:

(1) The WiFi DAQ system will be improved for more efficient power saving design and applications.

(2) Due to the pandemic, the experimental tests corresponding to rolling element fault have not been undertaken in this research. In the future, the performance of the proposed eTHT technique on ball element fault will be investigated.

(3) The proposed eTHT technique will be implemented for bearing fault detection in water pump stations in the Bare Point Water Treatment Plant in Thunder Bay, Ontario.

(4) Advanced research will be undertaken to optimize filter parameters and improve its robustness in general signal processing applications.

References

[1] A. Hasanbeigi, "U.S. Industrial Motor Systems Energy Efficiency Reports — Global Efficiency Intelligence", *Global Efficiency Intelligence*, 2017. [Online]. Available: https://www.globalefficiencyintel.com/us-industrial-motor-systems-ee-reports.

[2] W. T. Thomson and M. Fenger, "Current signature analysis to detect induction motor faults," *IEEE Industry Applications Magazine*, vol. 1, pp. 25-33, 2001

[3] P. Jansohn, A. Tejedor, R. Singh and P. Pilidis, *Modern gas turbine systems*, 1st ed. Woodhead Publishing, pp. 515-564, 2013.

[4] M. J. NEALE, *The tribology handbook*, 2nd ed. Oxford: Butterworth-Heinemann, pp. D11.1-D11.4, 1995.

[5] R. Isermann, *Fault-Diagnosis Systems*, *an introduction from fault detection to fault tolerance*, Darmstadt: Springer-Verlag Berlin Heidelberg, 2006.

[6] Rockwell Automation Inc, *Applying Condition Monitoring to Various Machinery*. Rockwell Automation, pp. 17-25, 2019.

[7] S. Bandyopadhyay, and E. J. Coyle, "An energy efficient hierarchical clustering algorithm for wireless sensor networks," in INFOCOM 2003. Twenty-Second Annual Joint Conference of the IEEE Computer and Communications. IEEE Societies, San Francisco, 2003.

[8] G. C. M. Meijer, *Smart Sensor Systems*, Chichester: John Wiley & Sons, Ltd, 2008

[9] W. Wang and O. A. Jianu, "A smart sensing unit for vibration measurement and monitoring," *IEEE/ASME Transactions on Mechatronics*, vol. 15, no. 1, pp. 70-79, 2010.

[10] S. Middelhoek, and A. C. Hoogerwerf, "Smart sensors: when and where?," *Sensors and Actuators*, vol. 8, no. 1, pp. 39-48, 1985.

[11] National Research Council, *Expanding the vision of sensor materials*. Washington, D.C: National Academy Press, pp. 9-18, 1995.

[12] P. Horowitz, *Winfield Hill The Art of Electronics*, Second Edition, Cambridge ISBN 0-521-37095-7 pages 462-464, 1989.

[13] L. Siret, "Data Acquisition," *Dewesoft.com*, 2020. [Online].
Available: https://dewesoft.com/daq/what-is-data-acquisition#data-storage. [Accessed:

22- Nov- 2020].

[14] Y. Kim, Y. Park, and J. Choi, "A study on the adoption of IoT smart home service: using value-based adoption model," *Total Quality Management and Business Excellence* , pp.1149–1165, 2017.

[15] H. Jo and Y. Yoon, "Intelligent smart home energy efficiency model using artificial TensorFlow engine," *Hum Centric Comput and Information Sciences.* 2018

[16] L. Hou, and N. W. Bergmann, "Novel industrial wireles sensor networks for machine condition monitoring and fault diagnosis," *IEEE Transactions on Instrumentation and Measurement*, vol. 61, no. 10, pp. 2787-2799, 2012.

[17] S. Nandi, H. A. Toliyat, and X. Li, "Condition monitoring and fault diagnosis of electrical motors – a review," *IEEE Transactions on energy Conversions*, vol. 20, no. 4, pp. 719-730, 2005

[18] T. Sengoz, "Online condition monitoring and fault detection in induction motorbearings," MSc Thesis, Lakehead University, Thunder Bay, Ontario, Canada, 2017

[19] T. Williams, X. Ribadeneria, and S. Billingtons, "Rolling element bearing diagnostics is run-to-failure lifetime testing, " *Mechanical System and Signal Processing*, vol.15, pp.979-993,2001.

[20] T. Miyachi and K. Seki, " An investigation of the early detection of defects in ball bearings using vibration monitoring- practical limit of detectability and growth speed of defects," Proceedings of the International Conference on Rotor dynamics, JSMEIFToMM, Tokyp, pp.402 -407, September 1986.

[21] R. Monk, "Vibration Measurement Gives Early Warning of Mechanical Faults." *Processing Engineering*, pp.135-137,Nov.1972.

[22] N. Tandon and B. Nakara, " Detection of defects in rolling element bearings by vibration monitoring," *Journal of the Institution of Engineers (India)- Mech EngDiv*, vol.37, pp.271-282,1993

[23] J. Mathew and R. Alfredson, "The condition monitoring of rolling element bearings using vibration analysis," *Trans ASME, Journal of Vibration and Acoustics,* vol. 106, pp.447-453,1984

[24] N. Tandon, "A comparison of some vibration parameters for the condition monitoring of

rolling element bearings," *Measurement*, vol. 12, pp. 285-289, 1994

[25] H. Ocak and K. A. Loparo, "HMM based fault detection and diagnosis scheme for rolling element bearings," *Trans ASME, Journal of Vibration and Acoustics*, vol. 127, pp. 300-306, 2005

[26] R. B. Randall, J. Antoni and S. Chobsaard, "A comparison of cyclostationary and envelope analysis in the diagnostics of rolling element bearings," 2000 IEEE International Conference on Acoustics, Speech, and Signal Processing. Proceedings (Cat. No.00CH37100), pp. 3882-3885 vol.6, 2000.

[27] D. Dyer and R. Stewart, "Detection of rolling element bearing damaged by statistical vibration analysis, " *Trans ASME, Journal of Mechanical Design*, vol. 100, pp.229-235, 1978.

[28] S. Osman and W. Wang, "An enhanced Hilbert-Huang transform technique for bearing condition monitoring", *Measurement Science and Technology*, vol. 24, (13pp), 2013

[29] S. Sassi, B. Badri and M. Thomas, "TALAF and THIKAT as innovative time domain indicators for tracking ball bearings", *In CMVA: Proceedings 24th seminar on machinery vibration*, pp. 413-417, 2006

[30] O. Yadav and G. L. Pahuja, "Bearing Health Assessment Using Time Domain Analysis of Vibration Signal," *International Journal of Image, Graphics and Signal Processing*; Hong Kong vol.12,lss.3,pp.27-40, 2020

[31] S. A Broughton and K. Bryan., Discrete Fourier Analysis and Wavelets: Applications to Signal and Image Processing. New York: Wiley. p. 72, 2008.

[32] B. Liang, S. D. Iwnicki and Y. Zhao, "Application of power spectrum, cepstrum, high order spectrum and neural network analysis for induction motor fault diagnosis," *Mechanical Systems and Signal Processing*, vol. 39, no. 1-2, pp. 342-360, 2013

[33] G. G. Yen and K. C. Lin, "Wavelet packet feature extraction for vibration monitoring, " *IEEE Transactions on Industrial Electronics*, vol.47, no. 3, pp. 650-667, 2000

[34] R. B. Randall, J. Antoni and S. Chobsaard, "The relationship between spectral correlation and envelope analysis in diagnostics of bearing faults and other cyclo-stationary machine signals," *Mechanical Systems and Signal Processing*, vol. 15, pp. 945-962, 2001

[35] D. Ho, R. B. Randall, "Optimization of bearing diagnostic techniques using simulated and actual bearing fault signals, " *Mechnical System Signal Process*, pp. 763-788, 2000.

[36] P. McFadden, J. Smith, "Vibration monitoring of rolling element bearings by the high frequency resonance technique of review," Tribol Int, pp. 3-10, 1984.

[37] N. Wang and X. Liu, "Bearing fault diagnosis method based on hilbert envelope demodulation analysis", *IOP Conference Series: Materials Science and Engineering*, vol. 436, p. 012009, 2018.

[38] R. Jiang, S. Liu, Y. Tang and Y. Liu, "A novel method of fault diagnosis for rolling element bearings based on the accumulated envelope spectrum of the wavelet packet, " *Journal of Vibration and Control*, vol. 21, no. 8, pp. 1580-1593, 2015

[39] J. Antoni, "The spectral kurtosis: a useful tool for characterizing non-stationary signals, " *Mechanical Systems and Signal Processing*, vol. 20, pp. 282-307, 2006

[40] Y. Ruqiang, RX. Gao, "Multi-scale enveloping spectrogram for vibration analysis in bearing defect diagnosis," *Tribology International*, Volume 42, Issue 2, pp293-302, 2009.

[41] K. Kumar, S. Shukla, S. K. Singh, "A combined approach for weak fault signature extraction of rolling element bearing using Hilbert envelop and zero frequency resonator, " *Journal of Sound and Vibration*, Volume 419, pp 436-451, 2018.

[42] H. Konstantin-Hansen, "Envelope analysis for diagnostics of local faults in rolling element bearings, " Brüel & Kjær Application Note, BO 0501, 2003

[43] S. Agarwal, S. R. Mohanty and V. Agarwal, "Bearing fault detection using hilbert and high frequency resolution techniques, " *IETE Journal of Research*, vol. 61, no. 2, pp. 99-108, 2015

[44] D. G. Childers, D. P. Skinner, R. C. Kemerait, "The Cepstrum: A Guide to Processing," *Proceedings of the IEEE*, Vol. 65, No. 10, pp. 1428–1443, October 1977.

[45] S. Prabhakar, A. R. Mohanty, A. S. Sekhar, "Application of discrete wavelet Transform for detection of ball bearing race faults, " *Tribology International*, Volume 35,Issue12, Pages 793-800, 2002.

[46] T. Kaewkongka Y. Au, R. Rakowski, and B. Jones, "A comparative study of short time fourier transform, and continuous wavelet transform for bearing condition monitoring, "

Internation Journal of COMADEM. Vol.6, pp 40-48, 2003.

[47] J. Liu, W. Wang and F. Ma, "Bearing system health condition monitoring using a wavelet cross-spectrum analysis technique," Journal of Vibration and Control, vol.11,pp.1-11, 2011.

[48] N. Huang, "The empirical mode decomposition and the Hilbert spectrum for nonlinear and non-stationary time series analysis," *Proceedings of the Royal Society of London. Series A: Mathematical, Physical and Engineering Sciences*, vol. 454, no. 1971, pp. 903-995, 1998. Available: 10.1098/rspa.1998.0193.

[49] K. Aida & M. Karim, "Bearing fault diagnosis using Hilbert-Huang transform (HHT) and support vector machine (SVM)," *Mechanics & Industry*. Vol.17, pp308, 2016.

[50] W. Zhidong, H. Rui, Z. Daokun, "The Fault Diagnosis of Rolling Bearing Based on MED and HHT," Proceedings of the International conference on logisticsm Engineeringmm Management and Computer Science, pp.278-282, 2015

[51] P. F. Pai, "Space wave number and time–frequency analyses for vibration and wave-based damage diagnosis," in Structural Health Monitoring (SHM) in Aerospace Structures, Y. FuhGuo, Ed. Woodhead Publishing, pp 393-426, 2016

[52] Z. Wu, N. Huang. "Ensemble empirical mode decomposition: a noise-assisted data analysis Method," *Advances in Adaptive Data Analysis*, vol. 1, pp.1-4. 2009.

[53] H. M. Teager, S. M. Teager, *A phenomenological model for vowel production in the vocal tract*, ch. 3, pp. 73-109. San Diego, CA: College-Hill Press, 1985.

[54] H. M. Teager, S. M. Teager, *Evidence for Nonlinear Sound Production Mechanisms in the Vocal Tract*, 55 of D, pp. 241-261. France: Kluwer Academic Publications, 1990.

[55] J. F. Kaiser, "On a simple algorithm to calculate the 'energy' of a signal," International Conference on Acoustics, Speech, and Signal Processing, Vol. 1, pp. 381-384, 1990.

[56] J. F. Kaiser, On Teager's energy algorithm and its generalization to continuous signals, Proceedings of IEEE DSP Workshop, 1990.

[57] I. Antoniadou, G. Manson, N. Dervilis,T. Barszcz, J. Staszewski, K. Worden, "A time-frequency analysis approach for condition monitoring of a wind turbine gearbox under varying load conditions," *Mech.Systems and Signal Process.*, Vol. 64-65, pp.188-216, 2015.

[58] R. B. Randall, "Wade A smith, Application of the Teager Kaiser Energy operator to Machine Diagnostics," Teenth DST Group International Conference on Health and Usage Monitoring System(HUMS). 2017

[59] N. Huang, *Hilbert-huang transform and its applications*, 2nd ed. WSPC, pp.1-26, 2014.

[60] Microchip. (2020) ATmega328P. [Online].

Available: https://www.microchip.com/wwwproducts/en/ATmega328p

[61] Microchip. (2020) 23LC1024: 2.5-5.5V 1Mb SPI Serial SRAM. [Online].

Available: https://www.microchip.com/wwwproducts/en/23LC1024

[62] Anaren. (2020) Wireless Transceivers: Air for Proprietary RF. [Online].

Available: https://www.anaren.com/catalog/wireless-transceivers/proprietary-rf

[63] D. Berenguer. (2014) Simple Wireless Abstract Protocol. [Online].

Available:https://github.com/panStamp/panstamp/wiki/Simple%20Wireless%20Abstract%20Protocol

[64] ESPRESSIF. (2020) SoCs: ESP32. [Online].

Available: https://www.espressif.com/en/products/socs/esp32-s2

[65] TEXAS INSTRUMENTS. (2020) ADS131A04 [Online].

Available: https://www.ti.com/product/ADS131A04

[66] W. Wang and A. Wong, "Autoregressive Model-Based Gear Fault Diagnosis", *Journal of Vibration and Acoustics*, vol. 124, no. 2, pp. 172-179, 2002.

[67] H. Endo and R. Randall, "Enhancement of autoregressive model based gear tooth fault detection technique by the use of minimum entropy deconvolution filter," *Mechanical Systems and Signal Processing*, vol. 21, no. 2, pp. 906-919, 2007.

[68] T. Barszcz and N. Sawalhi, "Fault Detection Enhancement in Rolling Element Bearings Using the Minimum Entropy Deconvolution", *Archives of Acoustics*, vol. 37, no. 2, 2012.

[69] W. Song, M. Li and J. Liang, "Prediction of Bearing Fault Using Fractional Brownian Motion and Minimum Entropy Deconvolution," *Entropy*, vol. 18, no. 11, p. 418, 2016.

[70] A. Rabah and K. Abdelhafid, "Rolling bearing fault diagnosis based on improved complete ensemble empirical mode of decomposition with adaptive noise combined with minimum entropy deconvolution, " *Journal of Vibroengineering*, vol. 20, no. 1, pp.

240-257, 2018.

[71] S. Robert and S. David. *Times series analysis and its applications: with R examples*, 3rd ed. Springer. ISBN 144197864X pp. 86-90, 2010.

[72] R. A. Wiggins, "Minimum entropy deconvolution, " *Geoexploration*, vol. 16, pp. 21-35, 1978.

[73] C. A. Cabrelli, "Minimum entropy deconvolution and simplicity: a noniterative algorithm," *Geophysics*, 50(3)(1985), pp. 394-413, 1985.

[74] G. L. McDonald and Q. Zhao, " Mutipoiont optimal minimum entropy deconvolution and convolution fix: Application to vibration fault detection," *Mechanical Systems and Signal Processing*, vol. 82, pp 461-477, 2017. [Abstract]. Available: https://www.sciencedirect.com/science/article/pii/S0888327016301297

[75] G. L. McDonald, Q. Zhao, and M. J. Zuo, "Maximum correlated kurtosis deconvolution and application on gear tooth chip fault detection," *Mechanical Systems and Signal Processing*, vol.33, pp 237-255, 2012. [Abstract]. Available: https://www.sciencedirect.com/science/article/pii/S0888327012002452

[76] P. Podder, T. Z. Khan, M. H. Khan and M. M. Rahman, "Comparative performance analysis of Hamming, Hanning and Blackman window," *International Journal of Computer Applications*, vol. 96, no. 18, pp. 1-7, 2014.

[77] W. V. Drongelen, *Signal Processing for Neuroscientists*, 1st ed. Cambridge: Academic Press, pp. Pages 55-70, 2007.

[78] R. G. Lyons, *Understanding Digital Signal Processing*, 3rd ed. Upper Saddle River: prentice Hall, pp. 590-597, 2004.

[79] "Apparatus & Procedures | Bearing Data Center", Csegroups.case.edu, 2021. [Online]. Available: https://csegroups.case.edu/bearingdatacenter/pages/apparatus-procedures.

[80] "SKF 6205 deep groove ball bearing", *Skf.com*,2021. [Online]. Available: https://www.skf.com/ca/en/products/rolling-bearings/ball-bearings/deep-groove-ball-bearings/productid-6205.